Wrinkle Generation without Bifurcation in a Shear-Enforced Rectangular Membrane with Free Boundaries

Kei Senda*, Mario Petrovic†, and Kei Nakanishi‡
Kyoto University, Kyoto 606-8501, Japan

The object of this study is to clarify wrinkling behavior of a shear-enforced flat rectangular membrane with free boundaries. For this purpose, an equilibrium path tracking method using a finite element method is developed. This method includes bifurcation path tracking analysis that searches for bifurcation solutions. This method establishes an image of membrane behavior by calculating a series of successive equilibrium states before and after bifurcation buckling. Through detailed analysis of stress, displacement fields, and wrinkle interaction over a load parameter range, the analysis shows how existing wrinkles affect each other and the generation of new wrinkles. As a result, there is wrinkle generation with bifurcation and without bifurcation. The wrinkle generation mechanism without bifurcation is analyzed in detail. Wrinkle generation caused by bifurcations could potentially result in a large number of equilibrium paths. Each equilibrium path represents a specific wrinkle pattern. However, the analyzed results show that significantly fewer equilibrium paths are obtained than expected. These are due to wrinkle generation without bifurcations and to deformation symmetry.

---

* Professor, Department of Aeronautics and Astronautics, Graduate School of Engineering, senda@kuaero.kyoto-u.ac.jp, Senior Member AIAA.
† Graduate Student, Department of Aeronautics and Astronautics, Graduate School of Engineering, mapetrov@live.com, Member AIAA
‡ Graduate Student, Department of Aeronautics and Astronautics, Graduate School of Engineering, keinakanishi5@gmail.com, Member AIAA

Nomenclature

a = length, m

b = width, m

D = Flexural rigidity, Nm^2

E = Young's Modulus, GPa

f = force, N

h = shell thickness, m

M = shell section moment, Nm/m

N = shell section force, N/m

q = displacement, m

t = time, s

u = displacement, m

δf = imposed force, N

δu = imposed displacement, m

ϵ = membrane strain

κ = curvature

λ = eigenvalue

ν = Poisson's ratio

ϕ = eigenvector

σ = membrane stress, $\mathrm{N/m}^2$

I. Introduction

When the structure and design of space vehicles are considered, weight and storage requirements are key limiting factors. Inflatable structures have attracted attention because such structures satisfy the above factors[1]. This study considers structures using deployable membranes. The structures are initially folded, deployed into their desired shape, unfolded or inflated, and rigidized.

The research goal of this study is to achieve stable deployment along a planned trajectory for a structure folded into a prescribed shape. However, because the structure is a membrane, with many

degrees of freedom, the prediction of membrane behavior is difficult. Here membrane behavior refers to displacement of membrane points under the effect of outside loads. In a deployment experiment using an inflatable tube[2], an origami-like pattern was designed to facilitate predictable deployment. However, small compressive forces cause local buckling and generate wrinkles. Buckling occurs after a bifurcation[3–6]. When a bifurcation occurs, the material may become unstable and the subsequent state may not be uniquely determined. This makes predicting stable deployment difficult. To solve this problem, an understanding of wrinkle behavior is essential.

In this study, a wrinkle is defined as an out-of-plane membrane deformation that occurs when a compressive load is applied to a membrane. Buckling is defined as a phenomenon generating a finite deformation in a direction different from the load applied to the structure.

An equilibrium state, or an equilibrium point, is defined as the static state of a membrane when a static load or an imposed displacement is applied. By varying a path parameter such as displacement or load, an equilibrium path is obtained, i.e. a sequence of equilibrium points. Bifurcation is a rapid equilibrium point shift and a qualitative change of the equilibrium state when the path parameter varies. A wrinkle, i.e. buckling of a membrane, is generated after a bifurcation. Therefore, in order to deploy a membrane structure along a planned trajectory, understanding of the bifurcation structure and the equilibrium paths is necessary.

The first step in analyzing wrinkling behavior is modeling the membrane structure. A continuum model based on partial differential equations and a Finite Element (FE) model are typical approaches, however the former yields solutions for only simple systems. Therefore, finite element modeling is used to analyze wrinkle behavior. In previous studies[7–9], membrane structures were modeled with membrane elements that ignore bending stiffness. The membrane element approach excels in terms of computational cost, however it can not accurately calculate out-of-plane deformation. By using shell elements that include bending stiffness, wrinkle amplitude and wavelength are calculated more accurately.

In a straight column or flat plate, the bifurcation after which buckling occurs is a branching bifurcation[3, 10]. For a flat membrane, it is believed that a wrinkle is generated by bifurcation and the number of wrinkles increases after bifurcation. A bifurcation is a singularity in the analysis.

Therefore, obtaining equilibrium points after bifurcation is difficult and numerous studies have been conducted[11]. A method for bifurcation path analysis is needed to obtain equilibrium points after bifurcation.

The arc length method, and the introduction of imperfections and dynamic analysis, are the common methods for path tracking after bifurcations[6, 12]. However, these methods do not always yield a solution, they change the bifurcation structure, or they obtain a fraction of paths after the bifurcation. To overcome this problem, a bifurcation path analysis method that is able to search for solutions after bifurcation is needed. In this study, a method of searching for bifurcation solutions is added into the equilibrium path tracking method, of Wagner and Wriggers[13].

Membrane wrinkling studies have mostly focused on certain effects on characteristics, i.e. gravity[14], creases[15], stress concentrations[16], etc. In general, wrinkling is analyzed as a membrane behavior event, and wrinkled geometry is computed for specific loads. The goal of this study is to obtain a comprehensive image/understanding of membrane wrinkling. For that purpose, several wrinkle generations, multiple wrinkle configurations, and wrinkle interaction will be considered.

In this study, a flat rectangular membrane with free boundary conditions is sheared, see Wong and Pellegrino[4] and Inoue[17]. In Wong and Pellegrino[5, 6] a wide range of numerical results were shown. This study uses bifurcation path tracking analysis to search for equilibrium points after bifurcations and to applies relatively small increments to imposed displacement for numerical analysis of the bifurcation structure and wrinkle behavior.

Wong and Pellegrino describe wrinkle generation in terms of bifurcations. Bifurcations generate multiple paths for wrinkle generation. Each bifurcation can increase the number of equilibrium paths. There are many possible deformation patterns when the membrane has many wrinkles.

In this study, the results show a membrane has an initial single equilibrium path that branches into 4 paths, then transitions into 2 paths and then again into 4 paths. When the first 4 paths exist, the number of wrinkles increases to 33 or 34 without bifurcations by increasing the prescribed displacement. This study clarifies a new wrinkle generation mechanism, in which wrinkles are generated at regular points on an equilibrium path. Because of this wrinkle mechanism, the branching

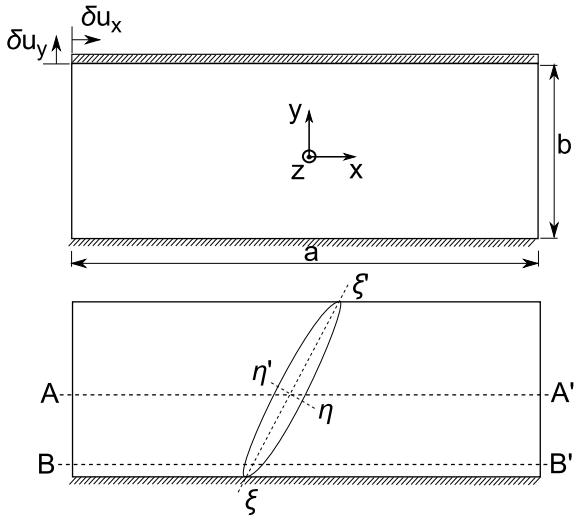

Fig. 1 Sheared rectangular membrane. Top and bottom edges have fixed boundaries. Right and left edges have free boundaries.

of the system is reduced and only a small number of paths exist. Two of the first 4 paths undergo bifurcations resulting in only 2 paths.

Additionally, system symmetry is discussed using the system's governing equations. This symmetry can be described as a dihedral group. Therefore, a single configuration results in three more configurations by applying these symmetrical transformations. However, symmetry in deformation patterns of a membrane reduces the number of configurations. Finally, a simpler bifurcation structure with fewer equilibrium paths, than expected based on the number of wrinkles is obtained.

This paper builds upon the previous work[18, 19] by improving the analysis method. The improved analysis method is used to obtain additional results and discuss the behavior in greater detail. The rest of this paper is organized as follows. Section II sets up the FEM model of a rectangular membrane using ABAQUS. A custom built subroutine functions as the path analysis method. Section III shows the path tracking method for a system with a prescribed displacement. Section IV introduces the solutions caused by symmetry, the similarity values and bifurcation diagrams. Section V presents some numerical simulations and discusses the results. Section VI presents concluding remarks.

Table 1 Membrane material properties.

Membrane width	a	0.30 [m]
Membrane height	b	0.10 [m]
Membrane thickness	h	12.5×10^{-6} [m]
Young's Modulus	E	3.0 [GPa]
Poisson's ratio	ν	0.3

II. Modeling and problem

A. Analyzed object and model

The membrane analyzed in this study is a flat membrane as illustrated in Fig. 1. The material is Kapton and its properties are listed in Table 1. The choice of a Kapton membrane comes from the flat membrane wrinkling data, e.g. Wong and Pellegrino[4] and Inoue[17]. The ratio of the horizontal and the vertical lengths $a : b$ is $3 : 1$. Fixed boundaries are set for the top and bottom edges, and free boundaries for the left and right edges. The fixed top edge is then subjected to a prescribed displacement. Gravity and imperfections are not considered.

The origin of the xyz-coordinate system is fixed at the membrane center of mass in the undeformed state, i.e. when no external loads are applied. The x-axis is parallel to the bottom edge, y-axis is perpendicular to the bottom edge, and z-axis is normal to the neutral plane, as defined in Fig. 1. Coordinates (x, y, z) refer to a position on the membrane prior to deformation, and they do not vary with deformation. Section AA' is defined at $y = 0$[m] and BB' at $y = -0.045$[m].

First, at the top fixed edge, a displacement of $\delta u_y = 30 \times 10^{-6}$[m] is applied in the y-direction and is constant throughout the analysis. This is to maintain consistency with experimental results in Inoue[17]. Then, an imposed displacement δu_x in x direction is applied. In this study, δu_x is increased from 0[m] to 650×10^{-6}[m].

Membrane deformation is described by displacements at all points on the membrane. Point displacements are represented by (u_x, u_y, u_z) in (x, y, z) coordinates. However, the z-displacement of points on the mid-plane is mainly considered, where displacement of a point in z-coordinate $u_z(x, y, 0)$ is simply expressed by $u_z(x, y)$. Stress and strain are given for the mid-plane. The tensile direction is positive for both stress and strain. Considering the plane stress, the $\xi\xi'$-axis corresponds to the first principal stress direction and the $\eta\eta'$-axis corresponds to the second principal stress

direction. When wrinkles exist, the $\xi\xi'$-axis in a the wrinkle longitudinal direction is perpendicular to $\eta\eta'$-axis. Both $\xi\xi'$ and $\eta\eta'$ rotate with the wrinkles and remain perpendicular to each other. A wrinkle is a sinusoidal shaped out-of-plane deformation that occurs between two points where curvature in η-direction changes sign.

The problems dealt with in this study are defined below. The membrane behavior is analyzed by increasing the imposed shear displacement δu_x. The behavior includes wrinkle geometry indicated by the displacement $u_z(x, y)$, bifurcation structure of the deformation, and stress. Stress values as well as forces and moments at certain points will be used to explain the behavior in more detail. The wrinkle generation mechanism is described by the following analysis.

B. Differential equations

The first step in the analysis of membrane wrinkling is establishing the governing equations for plates[3]. These equations provide the key properties of the system. For membranes, the Kirchhoff-Love assumptions for thin plates are adopted. By taking the standard plate definitions[3] the plate

equations are written as:

$$
\begin{aligned}
&\frac{Eh}{1-\nu^2}\left[\frac{\partial^2 u_x}{\partial x^2}+\frac{\partial u_z}{\partial x}\left(\frac{\partial^2 u_z}{\partial x^2}\right)+\nu\left\{\frac{\partial^2 u_y}{\partial x\partial y}+\frac{\partial u_z}{\partial y}\frac{\partial^2 u_z}{\partial x\partial y}\right\}\right]\\
&+\frac{Eh}{2(1+\nu)}\left\{\frac{\partial^2 u_x}{\partial y^2}+\frac{\partial^2 u_y}{\partial x\partial y}+\frac{\partial^2 u_z}{\partial x\partial y}\frac{\partial u_z}{\partial y}+\frac{\partial u_z}{\partial x}\frac{\partial^2 u_z}{\partial y^2}\right\}\\
&=f_x(u_x,\,u_y,\,u_z)=0 \qquad (1)\\
&\frac{Eh}{1-\nu^2}\left[\frac{\partial^2 u_x}{\partial y^2}+\frac{\partial u_z}{\partial y}\left(\frac{\partial^2 u_z}{\partial y^2}\right)+\nu\left\{\frac{\partial^2 u_x}{\partial x\partial y}+\frac{\partial u_z}{\partial x}\frac{\partial^2 u_z}{\partial x\partial y}\right\}\right]\\
&+\frac{Eh}{2(1+\nu)}\left\{\frac{\partial^2 u_y}{\partial x^2}+\frac{\partial^2 u_x}{\partial x\partial y}+\frac{\partial^2 u_z}{\partial x\partial y}\frac{\partial u_z}{\partial x}+\frac{\partial u_z}{\partial y}\frac{\partial^2 u_z}{\partial x^2}\right\}\\
&=f_y(u_x,\,u_y,\,u_z)=0 \qquad (2)\\
&-D\left(\frac{\partial^4 u_z}{\partial x^4}+\nu\frac{\partial^4 u_z}{\partial x^2\partial y^2}\right)-2D(1-\nu)\frac{\partial^4 u_z}{\partial x^2\partial y^2}-D\left(\frac{\partial^4 u_z}{\partial y^4}+\nu\frac{\partial^4 u_z}{\partial x^2\partial y^2}\right)\\
&+\frac{Eh}{1-\nu^2}\left\{\frac{\partial^2 u_x}{\partial x^2}+\frac{\partial^2 u_z}{\partial x^2}+\nu\left(\frac{\partial^2 u_x}{\partial x\partial y}+\frac{\partial u_z}{\partial y}\frac{\partial^2 u_z}{\partial x\partial y}\right)\right\}\frac{\partial u_z}{\partial x}\\
&+\frac{Eh}{2(1+\nu)}\left(\frac{\partial^2 u_x}{\partial x\partial y}+\frac{\partial^2 u_y}{\partial x^2}+\frac{\partial^2 u_z}{\partial x^2}\frac{\partial u_z}{\partial y}+\frac{\partial u_z}{\partial x}\frac{\partial^2 u_z}{\partial x\partial y}\right)\frac{\partial u_z}{\partial y}\\
&+\frac{Eh}{1-\nu^2}\left\{\frac{\partial^2 u_x}{\partial y^2}+\frac{\partial u_z}{\partial y}\frac{\partial^2 u_z}{\partial y^2}+\nu\left(\frac{\partial^2 u_x}{\partial x\partial y}+\frac{\partial^2 u_z}{\partial x\partial y}\right)\right\}\frac{\partial u_z}{\partial y}\\
&+\frac{Eh}{2(1+\nu)}\left(\frac{\partial^2 u_x}{\partial y^2}+\frac{\partial^2 u_y}{\partial x\partial y}+\frac{\partial^2 u_z}{\partial x\partial y}\frac{\partial u_z}{\partial y}+\frac{\partial u_z}{\partial x}\frac{\partial^2 u_z}{\partial y^2}\right)\frac{\partial u_z}{\partial x}\\
&=f_z(u_x,\,u_y,\,u_z)=0 \qquad (3)
\end{aligned}
$$

where the membrane flexural rigidity is defined as $D=\frac{Eh^3}{12(1-\nu^2)}$. The above equations are grouped as:

$$
\boldsymbol{f}(\boldsymbol{u}(\boldsymbol{x}))=\begin{bmatrix} f_x(u_x(x,\,y,\,z),\,u_y(x,\,y,\,z),\,u_z(x,\,y))\\ f_y(u_x(x,\,y,\,z),\,u_y(x,\,y,\,z),\,u_z(x,\,y))\\ f_z(u_x(x,\,y,\,z),\,u_y(x,\,y,\,z),\,u_z(x,\,y))\end{bmatrix}=\mathbf{0} \qquad (4)
$$

The boundary conditions are given by:

$$u_x(x,\,-\frac{b}{2},\,0)=0 \qquad u_y(x,\,-\frac{b}{2},\,0)=0 \qquad u_z(x,\,-\frac{b}{2},\,0)=0 \qquad (-\frac{3}{2}b\le x\le\frac{3}{2}b) \tag{5}$$

$$u_x(x,\,\frac{b}{2},\,0)=\delta u_x \qquad u_y(x,\,\frac{b}{2},\,0)=\delta u_y \qquad u_z(x,\,\frac{b}{2},\,0)=0 \qquad (-\frac{3}{2}b\le x\le\frac{3}{2}b) \tag{6}$$

$$\frac{\partial u_z}{\partial x}(x,\,\pm\frac{b}{2},\,0)=0 \qquad \frac{\partial u_z}{\partial y}(x,\,\pm\frac{b}{2},\,0)=0 \qquad \frac{\partial u_z}{\partial z}(x,\,\pm\frac{b}{2},\,0)=0 \qquad (-\frac{3}{2}b\le x\le\frac{3}{2}b) \tag{7}$$

$$\begin{aligned} N_{xx}(\pm\frac{3}{2}b,\,y,\,0) &= \frac{Eh}{1-\nu^2}\left[\frac{\partial u_x}{\partial x}+\frac{1}{2}\left(\frac{\partial u_z}{\partial x}\right)^2+\nu\left\{\frac{\partial u_y}{\partial y}+\frac{1}{2}\left(\frac{\partial u_z}{\partial y}\right)^2\right\}\right](\pm\frac{3}{2}b,\,y,\,0) \\ &= 0 \qquad (-\frac{b}{2}\le y\le\frac{b}{2}) \end{aligned} \tag{8}$$

While it is not possible to analytically solve these equations, they can be used to determine system symmetry to explain membrane behavior. This topic is discussed in a later section.

C. FEM model

The above geometry, properties and boundary conditions are modeled using ABAQUS. The S4R shell elements in ABAQUS are used. For the mesh, equal divisions in x and y directions are constructed resulting in 360×120 elements. The validity of this mesh density is discussed in Section V. It should be noted that only geometric nonlinearity is considered. Nonlinearity due to other factors such as material are not considered in the present study.

The static equilibrium of forces, i.e. nonlinear FE equations, $\boldsymbol{F}$, based on the displacement method, is formally written as:

$$\boldsymbol{F}(\boldsymbol{u},\,\boldsymbol{f})=\boldsymbol{0} \tag{9}$$

where $\boldsymbol{f}$ is the applied force for displacement $\boldsymbol{u}$. The static problem solves the equilibrium equation with δu_x for the equilibrium point $(\boldsymbol{u},\,\boldsymbol{f})$. The imposed displacement δu_x is included in $\boldsymbol{u}$ and the reaction forces for displacements $\boldsymbol{u}$ are included in $\boldsymbol{f}$. Equation (9) is a nonlinear equation for $\boldsymbol{u}$ and $\boldsymbol{f}$, which is difficult to solve. The solution method, e.g. an incremental calculation, is explained in the next section.

III. Equilibrium path tracking method

For equilibrium path tracking, a new equilibrium point, near the current equilibrium point, is determined by slightly changing the path parameter. However, if the new point is a bifurcation point, a bifurcation path analysis method is needed to search for post-bifurcation points because a bifurcation point is a singularity in the analysis. A bifurcation diagram shows the relative position of equilibrium points before and after the bifurcation point. The bifurcation diagram and deformation must be obtained in order to understand membrane behavior at the bifurcation points within path parameters.

First, from an analytical standpoint, the possible bifurcation structures will be discussed based on the asymptotic theory discussed in Endo[20] where the path parameter is load. Because the path parameter in this study is displacement, the relation between load and displacement is established. The relationship between the deformed state of the membrane $\boldsymbol{u}$ and the incremental displacement δu_x will be established, where the displacement δu_x is the path parameter. Finally, a method for searching for bifurcation solutions equivalent to that of Wagner and Wriggers[13] is built into the equilibrium path tracking method. This search consists of a stability inspection of the tangent stiffness matrix. Near bifurcation points the relevant eigenvectors are used to obtain bifurcation solutions. The process will be discussed in more detail later on.

Because this study does not consider imperfections, the following discussion about bifurcation points will be based on perfect bifurcations. If imperfections are considered, the bifurcation structure changes. A bifurcation point is removed and the equilibrium path that led to the bifurcation point now connects directly into one of the post-bifurcation paths. Instead of branching paths after a bifurcation, the imperfections select one path. Gravity has a similar effect; it acts as a disturbance that selects a single path at a bifurcation. By considering these effects, bifurcation is reduced to a single continuous equilibrium path.

A. Successive solution calculation

For successive solutions to nonlinear equations, the relationship between increments of $\boldsymbol{f}$ and $\boldsymbol{u}$ is shown. The relationship to incremental δu_x will be discussed later.

An equilibrium point $(\boldsymbol{u}_0 + \tilde{\boldsymbol{u}},\ \boldsymbol{f}_0 + \tilde{\boldsymbol{f}})$ close to a given equilibrium point $(\boldsymbol{u}_0,\ \boldsymbol{f}_0)$ of Eq. (9) satisfies

$$\boldsymbol{F}(\boldsymbol{u}_0 + \tilde{\boldsymbol{u}},\ \boldsymbol{f}_0 + \tilde{\boldsymbol{f}}) = \boldsymbol{0} \tag{10}$$

Expanding Eq. (10) in a Taylor series and by omitting the higher order terms gives

$$\boldsymbol{K}\tilde{\boldsymbol{u}} = \tilde{\boldsymbol{f}} \tag{11}$$

where $\boldsymbol{K} = \dfrac{\partial \boldsymbol{F}}{\partial \boldsymbol{u}^T}$ is the tangent stiffness matrix and $-\dfrac{\partial \boldsymbol{F}}{\partial \boldsymbol{f}^T}$ is the unit matrix.

A solution at the new equilibrium point,$(\boldsymbol{u}_0 + \tilde{\boldsymbol{u}},\ \boldsymbol{f}_0 + \tilde{\boldsymbol{f}})$ of the original nonlinear equation (10) is determined by iterative methods, e.g. Newton-Raphson method. This is the equilibrium path tracking method that seeks successive equilibrium points by gradually increasing $\boldsymbol{f}$ (or δu_x). Also, it is the static solution method that obtains solutions satisfying the static equilibrium equation (9). However, at the structure bifurcation point that is a singular point $(\boldsymbol{u}_c, \boldsymbol{f}_c)$, $\det \boldsymbol{K} = 0$, and the incremental displacement $\tilde{\boldsymbol{u}}$ corresponding to incremental load $\tilde{\boldsymbol{f}}$ cannot be uniquely determined. In this case, a bifurcation path analysis that searches for post-bifurcation paths is needed.

B. Asymptotic theory of bifurcation analysis

In order to correctly track paths after a bifurcation, a prediction of the bifurcation structure and post-bifurcation behavior is desired. Some bifurcation analyses based on asymptotic theory have been presented[20]. Although they are for static loads, they are helpful. Because experiments usually use imposed displacements, an asymptotic theory of bifurcation analysis for imposed displacement is needed. The following is an overview of bifurcation analysis for a static load.

1. Nonlinear equation solution

An equilibrium of a system is represented by Eq. (9). The equilibrium points are calculated by the Newton-Raphson method, which is an iterative method to solve nonlinear equations (9). An equilibrium point $(\boldsymbol{u}_*,\ f_*)$ is calculated close to the given equilibrium point $(\boldsymbol{u}^{(i)},\ f_i)$. By setting

$(\boldsymbol{u}_*,\, f_*) = (\boldsymbol{u}^{(i)} + \tilde{\boldsymbol{u}}^{(i+1)},\, f_*)$, the following equation for $i = 0, 1, 2, 3, \ldots$ is obtained.

$$\boldsymbol{F}(\boldsymbol{u}^{(i)} + \tilde{\boldsymbol{u}}^{(i+1)},\, f_*) = \boldsymbol{F}(\boldsymbol{u}^{(i)},\, f_*) + \frac{\partial \boldsymbol{F}}{\partial \boldsymbol{u}^T}(\boldsymbol{u}^{(i)})\tilde{\boldsymbol{u}}^{(i+1)} + \frac{1}{2!}\tilde{\boldsymbol{u}}^{(i+1)\ T}\frac{\partial^2 \boldsymbol{F}}{\partial \boldsymbol{u}\partial \boldsymbol{u}^T}(\boldsymbol{u}^{(i)})\tilde{\boldsymbol{u}}^{(i+1)} + \cdots = \boldsymbol{0} \tag{12}$$

where higher order terms are omitted. Rearranging gives:

$$\tilde{\boldsymbol{u}}^{(i+1)} \approx -\boldsymbol{K}_i^{-1}\boldsymbol{F}(\boldsymbol{u}^{(i)},\, f_*) \tag{13}$$

where $\boldsymbol{K}_i = \dfrac{\partial \boldsymbol{F}}{\partial \boldsymbol{u}^T}(\boldsymbol{u}^{(i)})$ is the tangent stiffness matrix at $\boldsymbol{u}^{(i)}$.

Calculation of $\boldsymbol{F}(\boldsymbol{u}^{(1)},\, f_*)$, $\boldsymbol{F}(\boldsymbol{u}^{(2)}, f_*)$, $\ldots$, $\boldsymbol{F}(\boldsymbol{u}^{(n)},\, f_*)$ is performed until $\boldsymbol{F}(\boldsymbol{u}^{(n)},\, f_*) = \boldsymbol{0}$.

2. Asymptotic theory near the bifurcation point

When determinants of the tangent stiffness matrices $\boldsymbol{K}_0$, $\boldsymbol{K}_1$, $\boldsymbol{K}_2$, $\ldots$ are zero, $\tilde{\boldsymbol{u}}^{(1)}$, $\tilde{\boldsymbol{u}}^{(2)}$, $\tilde{\boldsymbol{u}}^{(3)}$, $\ldots$ cannot be determined uniquely. At a bifurcation point, the tangent stiffness matrix has at least one zero eigenvalue. Solution $(\boldsymbol{u}^{(i)},\, f_i)$ is called a simple singular point when tangent stiffness matrix $\boldsymbol{K}_i$ has one zero eigenvalue. Following Endo, et al[20], a bifurcation point $(\boldsymbol{u}_c,\, f_c)$ that is a simple singular point is discussed. At a bifurcation point $(\boldsymbol{u}_c,\, f_c)$, the expanded incremental equation based on Eq. (9) becomes:

$$\boldsymbol{F}(\boldsymbol{u}_c,\, f_c) + \boldsymbol{K}_c\tilde{\boldsymbol{u}} + \boldsymbol{I}\tilde{f} + \cdots - \boldsymbol{F}(\boldsymbol{u}_c,\, f_c) = \boldsymbol{0} \tag{14}$$

where $||\tilde{\boldsymbol{u}}|| \ll 1$, $|\tilde{f}| \ll 1$. The eigenvalues and the corresponding eigenvectors of $\boldsymbol{K}_c$, respectively, are $\lambda_1, \lambda_2, \ldots, \lambda_n$ and $\boldsymbol{\phi}_1, \boldsymbol{\phi}_2, \ldots, \boldsymbol{\phi}_n$ which are normalized. All eigenvalues are real and $\lambda_1 = 0$.

The basis matrix is $\boldsymbol{\Phi}$ and incremental displacement vector $\tilde{\boldsymbol{u}}$ is approximated as:

$$\tilde{\boldsymbol{u}} = \boldsymbol{\Phi}\tilde{\boldsymbol{q}} = \begin{bmatrix} \boldsymbol{\phi}_1 & \boldsymbol{\phi}_2 & \cdots & \boldsymbol{\phi}_n \end{bmatrix} \begin{bmatrix} \tilde{q}_1 \\ \tilde{q}_2 \\ \vdots \\ \tilde{q}_n \end{bmatrix} \tag{15}$$

$$\frac{\partial \boldsymbol{F}}{\partial \boldsymbol{u}^T}(\boldsymbol{u}_c,\, f_c) = \left(\frac{\partial \boldsymbol{F}}{\partial \boldsymbol{u}^T}\right)_c = \boldsymbol{K}_c \tag{16}$$

$$= \boldsymbol{\Phi} \begin{bmatrix} \frac{\partial^{\phi}F_1}{\partial^{\phi}u_1} & \frac{\partial^{\phi}F_1}{\partial^{\phi}u_2} & \cdots & \frac{\partial^{\phi}F_1}{\partial^{\phi}u_n} \\ \frac{\partial^{\phi}F_2}{\partial^{\phi}u_1} & \frac{\partial^{\phi}F_2}{\partial^{\phi}u_2} & \cdots & \frac{\partial^{\phi}F_2}{\partial^{\phi}u_n} \\ \vdots & \vdots & \ddots & \vdots \\ \frac{\partial^{\phi}F_n}{\partial^{\phi}u_1} & \frac{\partial^{\phi}F_n}{\partial^{\phi}u_2} & \cdots & \frac{\partial^{\phi}F_n}{\partial^{\phi}u_n} \end{bmatrix} \boldsymbol{\Phi}^T = \boldsymbol{\Phi} \begin{bmatrix} \lambda_1 & 0 & \cdots & 0 \\ 0 & \lambda_2 & \cdots & 0 \\ \vdots & \vdots & \ddots & \vdots \\ 0 & 0 & \cdots & \lambda_n \end{bmatrix} \boldsymbol{\Phi}^T \tag{17}$$

The coordinate transformation of Eq. (15) yields

$$\boldsymbol{\Phi}^T \left(\boldsymbol{F}(\boldsymbol{u}_c + \tilde{\boldsymbol{u}},\, f_c + \tilde{f}) - \boldsymbol{F}(\boldsymbol{u}_c,\, f_c)\right) = \boldsymbol{0} \tag{18}$$

$${}^{\Phi}\boldsymbol{K}_c\tilde{\boldsymbol{q}} + \boldsymbol{\Phi}^T \left(\frac{\partial \boldsymbol{F}}{\partial f}\right)_c \tilde{f} + \cdots = \boldsymbol{0} \tag{19}$$

$$\begin{bmatrix} \lambda_1\tilde{q}_1 + \boldsymbol{\phi}_1^T \left(\frac{\partial \boldsymbol{F}}{\partial f}\right)_c \tilde{f} + \cdots \\ \lambda_2\tilde{q}_2 + \boldsymbol{\phi}_2^T \left(\frac{\partial \boldsymbol{F}}{\partial f}\right)_c \tilde{f} + \cdots \\ \vdots \\ \lambda_n\tilde{q}_n + \boldsymbol{\phi}_n^T \left(\frac{\partial \boldsymbol{F}}{\partial f}\right)_c \tilde{f} + \cdots \end{bmatrix} = \begin{bmatrix} \tilde{F}_1(\tilde{\boldsymbol{q}}, \tilde{f}) \\ \tilde{F}_2(\tilde{\boldsymbol{q}}, \tilde{f}) \\ \vdots \\ \tilde{F}_n(\tilde{\boldsymbol{q}}, \tilde{f}) \end{bmatrix} = \boldsymbol{0} \tag{20}$$

The solution for the incremental displacements is:

$$\tilde{q_2} = -\frac{1}{\lambda_2}\left(\boldsymbol{\phi}_2^T \left(\frac{\partial \boldsymbol{F}}{\partial f}\right)_c \tilde{f} + \cdots\right) \tag{21}$$

$$\vdots$$

$$\tilde{q}_n = -\frac{1}{\lambda_n}\left(\boldsymbol{\phi}_n^T \left(\frac{\partial \boldsymbol{F}}{\partial f}\right)_c \tilde{f} + \cdots\right) \tag{22}$$

The generalized displacement $\tilde{q}_2$, $\tilde{q}_3$, …, $\tilde{q}_n$ can be eliminated, since they are the incremental displacements components associated with the non-zero eigenvalues. By substituting $\tilde{q}_2$, $\tilde{q}_3$, …, $\tilde{q}_n$

functions of $\tilde{q}_1$ and $\tilde{f}$ into Eq. (20), the following equation is obtained.

$$\tilde{F}_1(\tilde{\boldsymbol{q}}, \tilde{f}) = \tilde{F}_1(\tilde{q}_1, \tilde{f}) = 0 \tag{23}$$

Equation (23) is expanded into a Taylor series, which yields

$$\tilde{F}_1(0, 0) + \sum_{i=1}^{n} \frac{1}{i!} \frac{\partial^i \tilde{F}_1}{\partial \tilde{q}_1^i} \tilde{q}_1^i + \sum_{i=1}^{n} \frac{1}{i!} \frac{\partial^i \tilde{F}_1}{\partial \tilde{f}^i} \tilde{f}^i + \sum_{i=1}^{n} \sum_{j=1}^{n} \frac{1}{(i+j)!} \frac{\partial^{i+j} \tilde{F}_1}{\partial \tilde{q}_1^i \partial \tilde{f}^j} \tilde{q}_1^i \tilde{f}^j = 0 \tag{24}$$

$$A_{00} + (A_{10}\tilde{q}_1 + \cdots) + (A_{01}\tilde{f} + \cdots) + (A_{11}\tilde{q}_1\tilde{f} + \cdots) = 0 \tag{25}$$

$$A_{ij} = \frac{1}{i!j!} \frac{\partial^{i+j}}{\partial \tilde{q_1}^i \partial \tilde{f}^j} \tilde{F}_1(0, 0) \tag{26}$$

3. Classification of bifurcation points

A tangent stiffness matrix has one zero eigenvalue, and the following conditions are assumed:

$$|\tilde{q}_1| = O(\delta),\ |\tilde{f}| = O(\epsilon),\ 0 < \epsilon \ll 1,\ 0 < \delta \ll 1 \tag{27}$$

$$\lambda_1 = 0,\ \lambda_2 = \cdots = \lambda_n = O(1) \tag{28}$$

$$A_{ij} = O(1) \tag{29}$$

$$\boldsymbol{\phi}_i^T \left(\frac{\partial \boldsymbol{F}}{\partial f} \right)_c = O(1) \quad (i = 2, 3, \ldots, n) \tag{30}$$

According to the asymptotic theory, there exist the following bifurcation points: (i)-a limit point, i.e. maximum or minimum point, (i)-b limit point, i.e. inflection point, (ii)-a asymmetric bifurcation point, and (ii)-b symmetric bifurcation point. The relation between the incremental displacement and the loading parameter is analyzed in each case.

(i)-a Snap-through bifurcation point (maximum and minimum point)

If $\epsilon \sim \delta^2 \ll \delta$, Eq. (25) is rearranged as:

$$A_{20}\tilde{q}_1^2 + A_{01}\tilde{f} = 0 \tag{31}$$

Eqs. (21) to (22) become

$$\tilde{q_2} \sim -\frac{1}{\lambda_2}\boldsymbol{\phi}_2^T \left(\frac{\partial \boldsymbol{F}}{\partial f}\right)_c \tilde{f} = O(\tilde{f}) \ll O(\tilde{q}_1) \tag{32}$$

$$\vdots$$

$$\tilde{q}_n \sim -\frac{1}{\lambda_n}\boldsymbol{\phi}_n^T \left(\frac{\partial \boldsymbol{F}}{\partial f}\right)_c \tilde{f} = O(\tilde{f}) \ll O(\tilde{q}_1) \tag{33}$$

Considering assumption $\tilde{q}_1 \gg \tilde{f}$, Eq. (15) yields the direction of the bifurcation path as:

$$\tilde{\boldsymbol{u}} = \left[\begin{array}{cccc} \boldsymbol{\phi}_1 & \boldsymbol{\phi}_2 & \cdots & \boldsymbol{\phi}_n \end{array}\right] \left[\begin{array}{c} \tilde{q}_1 \\ \tilde{q}_2 \\ \vdots \\ \tilde{q}_n \end{array}\right] \tag{34}$$

$$\sim \tilde{q}_1 \boldsymbol{\phi}_1 \tag{35}$$

Therefore, $\tilde{\boldsymbol{u}} \approx \tilde{q}_1\boldsymbol{\phi}_1$ is satisfied near the bifurcation points. The force $\tilde{f}$ is a quadratic function of $\tilde{q}_1$, and the bifurcation point is the extremal value of the function. So, $\tilde{q}_1$ changes rapidly for a slight change of $\tilde{f}$.

(i)-b Snap-through bifurcation point (inflection point) ($A_{20} = 0$)

If $\epsilon \sim \delta^3 \ll \delta$, Eq. (25) is rearranged as:

$$A_{30}\tilde{q}_1^3 + A_{01}\tilde{f} = 0 \tag{36}$$

Here, $\tilde{\boldsymbol{u}} \approx \tilde{q}_1\boldsymbol{\phi}_1$ is also satisfied near the bifurcation points. The force $\tilde{f}$ is a cubic function of $\tilde{q}_1$, and the bifurcation point is the inflection point of the function. So, $\tilde{q}_1$ changes rapidly after a slight change of $\tilde{f}$.

(ii)-a Asymmetric bifurcation point ($A_{01} = 0$, $A_{20}A_{02} - \frac{1}{4}A_{11} < 0$)

If $\epsilon^2 \ll \delta\epsilon \sim \delta^2 \ll \epsilon \ll \delta$, Eq. (25) is rearranged as:

$$A_{20}\tilde{q}_1^2 + A_{11}\tilde{q}_1\tilde{f} = 0 \tag{37}$$

Here, $\tilde{\boldsymbol{u}} \approx \tilde{q}_1\boldsymbol{\phi}_1$ is also satisfied near the bifurcation points. This results in $\tilde{q}_1 = 0$ or $\tilde{q}_1$ is a linear function of $\tilde{f}$. $\tilde{q}_1 = 0$ is the primary path. The linear function $A_{20}\tilde{q}_1 + A_{11}\tilde{f} = 0$ is the bifurcation path. At the bifurcation path, $\tilde{q}_1$ is the same order of $\tilde{f}$.

(ii)-b Symmetric bifurcation point ($A_{01} = A_{20} = 0$, $A_{20}A_{02} - \frac{1}{4}A_{11} < 0$)

If $\epsilon^2 \ll \delta^3 \sim \delta\epsilon \ll \epsilon \ll \delta$, Eq. (25) is rearranged as:

$$A_{30}\tilde{q}_1^3 + A_{11}\tilde{q}_1\tilde{f} = 0 \tag{38}$$

Here, $\tilde{\boldsymbol{u}} \approx \tilde{q}_1\boldsymbol{\phi}_1$ is also satisfied near the bifurcation points. This results in $\tilde{q}_1 = 0$ or $\tilde{q}_1$ is quadratic function of $\tilde{f}$. $\tilde{q}_1 = 0$ is the primary path and a quadratic function $A_{30}\tilde{q}_1^2 + A_{11}\tilde{f} = 0$ is the bifurcation path. So, $\tilde{q}_1$ changes rapidly for a slight change of $\tilde{f}$.

C. imposed displacement and imposed load relation

In this subsection, the analysis method based on nonlinear equations for imposed displacements will be explained in terms of asymptotic theory.

The governing nonlinear equations is Eq. (9) where the displacement vector $\boldsymbol{u}$, and the external force vector $\boldsymbol{f}$ are defined as:

$$\boldsymbol{u} = \begin{bmatrix} \underline{\boldsymbol{u}}_1 \\ \underline{\boldsymbol{u}}_{2f} \\ \boldsymbol{u}_{2nof} \end{bmatrix}, \quad \boldsymbol{f} = \begin{bmatrix} \boldsymbol{f}_1 \\ \boldsymbol{f}_{2f} \\ \underline{\boldsymbol{f}}_{2nof} \end{bmatrix} \tag{39}$$

where the underlined variables are prescribed and those with suffixes 1 and 2 correspond to geometric boundary conditions and loads as mechanical boundary conditions, respectively. In addition, $\underline{\boldsymbol{u}}_1$

represents the y and z degrees of freedom at the top boundary and the x, y and z degrees of freedom at the bottom boundary, therefore $\underline{\boldsymbol{u}}_1 = \mathbf{0}$.

The term $\underline{\boldsymbol{u}}_{2f}$ are the degrees of freedom on the top boundary in x-direction. The term $\boldsymbol{u}_{2nof}$ represents the degrees of freedom of all nodes except at the top and bottom boundaries. Force $\boldsymbol{f}_1$ is the load that is applied to maintain the constraint $\underline{\boldsymbol{u}}_1 = \mathbf{0}$. The term $\boldsymbol{f}_{2f}$ is the load generated by the imposed $\underline{\boldsymbol{u}}_{2f}$. The term $\underline{\boldsymbol{u}}_{2f}$ is a M size vector and $\boldsymbol{u}_{2nof}$ is a N size vector.

The $\underline{\boldsymbol{f}}_{2nof}$ term is the external force on the degrees of freedom in $\boldsymbol{u}_{2nof}$, however there is no external force on them, hence $\underline{\boldsymbol{f}}_{2nof} = \mathbf{0}$. The original nonlinear equation becomes:

$$\boldsymbol{F}(\underline{\boldsymbol{u}}_1,\, \underline{\boldsymbol{u}}_{2f},\, \boldsymbol{u}_{2nof},\, \boldsymbol{f}_1,\, \boldsymbol{f}_{2f},\, \underline{\boldsymbol{f}}_{2nof}) = \mathbf{0} \tag{40}$$

By dividing this into this three parts, i.e. the fixed boundary, the boundary with the imposed displacement and the other parts, the nonlinear equations are rewritten as:

$$\boldsymbol{F}_1(\underline{\boldsymbol{u}}_1,\, \underline{\boldsymbol{u}}_{2f},\, \boldsymbol{u}_{2nof},\, \boldsymbol{f}_1) = \mathbf{0} \tag{41}$$

$$\boldsymbol{F}_{2f}(\underline{\boldsymbol{u}}_1,\, \underline{\boldsymbol{u}}_{2f},\, \boldsymbol{u}_{2nof},\, \boldsymbol{f}_{2f}) = \mathbf{0} \tag{42}$$

$$\boldsymbol{F}_{2nof}(\underline{\boldsymbol{u}}_1,\, \underline{\boldsymbol{u}}_{2f},\, \boldsymbol{u}_{2nof},\, \underline{\boldsymbol{f}}_{2nof}) = \mathbf{0} \tag{43}$$

Now a coordinate transformation is performed. By considering the generalized coordinates in x-direction at the top edge, the transformation is:

$$\underline{\boldsymbol{u}}_{2f} = \begin{bmatrix} 1 & 0 & \cdots & 0 & 1 \\ 0 & 1 & \cdots & 0 & 1 \\ \vdots & \vdots & \ddots & \vdots & \vdots \\ 0 & 0 & \cdots & 1 & 1 \\ 0 & 0 & \cdots & 0 & 1 \end{bmatrix} \begin{bmatrix} \underline{u}_{2f1} - \underline{u}_{2fM} \\ \underline{u}_{2f2} - \underline{u}_{2fM} \\ \vdots \\ \underline{u}_{2fM-1} - \underline{u}_{2fM} \\ \underline{u}_{2fM} \end{bmatrix} = \boldsymbol{T}\underline{\boldsymbol{u}}'_{2f}$$

As shown in the equation, the new coordinates are described by the original coordinates $\boldsymbol{u}_{2f}$ and the equation can be solved for $\underline{\boldsymbol{u}}'_{2f}$ in reverse, thus $\underline{\boldsymbol{u}}'_{2f}$ is also a generalized coordinate. Substituting

this relation into the above equations, considering the constraint condition $\underline{\boldsymbol{u}}_{2f} = \delta\underline{u}_x\underline{\boldsymbol{e}}$, and the vector $\underline{\boldsymbol{c}}$ as the constant vector:

$$\underline{\boldsymbol{c}} = [0 \quad \cdots \quad 0 \quad 1]^T \tag{44}$$

the Taylor expansion by using the relationships $\underline{\boldsymbol{u}}_{2f} = \boldsymbol{T}\underline{\boldsymbol{u}}_{2f}^{'} = \boldsymbol{T}\underline{\boldsymbol{c}}\delta\underline{u}_x$ is performed:

$$\frac{\partial \boldsymbol{F}_1}{\partial \underline{\boldsymbol{u}}_1^T}\tilde{\underline{\boldsymbol{u}}}_1 + \frac{\partial \boldsymbol{F}_1}{\partial \boldsymbol{u}_{2f}^T}\boldsymbol{T}\underline{\boldsymbol{c}}\delta\tilde{\underline{u}}_x + \frac{\partial \boldsymbol{F}_1}{\partial \boldsymbol{u}_{2nof}^T}\tilde{\boldsymbol{u}}_{2nof} + \frac{\partial \boldsymbol{F}_1}{\partial \boldsymbol{f}_1^T}\tilde{\boldsymbol{f}}_1 + \cdots = \boldsymbol{0} \tag{45}$$

$$\frac{\partial \boldsymbol{F}_{2f}}{\partial \underline{\boldsymbol{u}}_1^T}\tilde{\underline{\boldsymbol{u}}}_1 + \frac{\partial \boldsymbol{F}_{2f}}{\partial \boldsymbol{u}_{2f}^T}\boldsymbol{T}\underline{\boldsymbol{c}}\delta\tilde{\underline{u}}_x + \frac{\partial \boldsymbol{F}_{2f}}{\partial \boldsymbol{u}_{2nof}^T}\tilde{\boldsymbol{u}}_{2nof} + \frac{\partial \boldsymbol{F}_{2f}}{\partial \boldsymbol{f}_{2f}^T}\tilde{\boldsymbol{f}}_{2f} + \cdots = \boldsymbol{0} \tag{46}$$

$$\frac{\partial \boldsymbol{F}_{2nof}}{\partial \underline{\boldsymbol{u}}_1^T}\tilde{\underline{\boldsymbol{u}}}_1 + \frac{\partial \boldsymbol{F}_{2nof}}{\partial \boldsymbol{u}_{2f}^T}\boldsymbol{T}\underline{\boldsymbol{c}}\delta\tilde{\underline{u}}_x + \frac{\partial \boldsymbol{F}_{2nof}}{\partial \boldsymbol{u}_{2nof}^T}\tilde{\boldsymbol{u}}_{2nof} + \frac{\partial \boldsymbol{F}_{2nof}}{\partial \underline{\boldsymbol{f}}_{2nof}^T}\tilde{\underline{\boldsymbol{f}}}_{2nof} + \cdots = \boldsymbol{0} \tag{47}$$

Here, the addition of the tilde notation is to indicate that the increments occur at the bifurcation point, as is discussed in Section III B 2. The linear parts are rewritten in matrix forms as:

$$\begin{bmatrix} \frac{\partial \boldsymbol{F}_1}{\partial \underline{\boldsymbol{u}}_1^T} & \frac{\partial \boldsymbol{F}_1}{\partial \boldsymbol{u}_{2f}^T}\boldsymbol{T} & \frac{\partial \boldsymbol{F}_1}{\partial \boldsymbol{u}_{2nof}^T} \\ \frac{\partial \boldsymbol{F}_{2f}}{\partial \underline{\boldsymbol{u}}_1^T} & \frac{\partial \boldsymbol{F}_{2f}}{\partial \boldsymbol{u}_{2f}^T}\boldsymbol{T} & \frac{\partial \boldsymbol{F}_{2f}}{\partial \boldsymbol{u}_{2nof}^T} \\ \frac{\partial \boldsymbol{F}_{2nof}}{\partial \underline{\boldsymbol{u}}_1^T} & \frac{\partial \boldsymbol{F}_{2nof}}{\partial \boldsymbol{u}_{2f}^T}\boldsymbol{T} & \frac{\partial \boldsymbol{F}_{2nof}}{\partial \boldsymbol{u}_{2nof}^T} \end{bmatrix} \begin{bmatrix} \tilde{\underline{\boldsymbol{u}}}_1 \\ \underline{\boldsymbol{c}}\delta\tilde{\underline{u}}_x \\ \tilde{\boldsymbol{u}}_{2nof} \end{bmatrix} = \begin{bmatrix} \tilde{\boldsymbol{f}}_1 \\ \tilde{\boldsymbol{f}}_{2f} \\ \tilde{\underline{\boldsymbol{f}}}_{2nof} \end{bmatrix} \tag{48}$$

or:

$$\begin{bmatrix} \boldsymbol{K}_{11} & \boldsymbol{K}_{12}\boldsymbol{T} & \boldsymbol{K}_{13} \\ \boldsymbol{K}_{21} & \boldsymbol{K}_{22}\boldsymbol{T} & \boldsymbol{K}_{23} \\ \boldsymbol{K}_{31} & \boldsymbol{K}_{32}\boldsymbol{T} & \boldsymbol{K}_{33} \end{bmatrix} \begin{bmatrix} \tilde{\underline{\boldsymbol{u}}}_1 \\ \underline{\boldsymbol{c}}\delta\tilde{\underline{u}}_x \\ \tilde{\boldsymbol{u}}_{2nof} \end{bmatrix} = \begin{bmatrix} \tilde{\boldsymbol{f}}_1 \\ \tilde{\boldsymbol{f}}_{2f} \\ \tilde{\underline{\boldsymbol{f}}}_{2nof} \end{bmatrix} \tag{49}$$

The boundary conditions $\tilde{\underline{\boldsymbol{u}}}_1 = \boldsymbol{0}$, $\tilde{\underline{\boldsymbol{f}}}_{2nof} = \boldsymbol{0}$ transform the equation into:

$$\begin{bmatrix} \boldsymbol{K}_{22}^{'} & \boldsymbol{k}_{22} & \boldsymbol{K}_{23} \\ \boldsymbol{K}_{32}^{'} & \boldsymbol{k}_{32} & \boldsymbol{K}_{33} \end{bmatrix} \begin{bmatrix} \boldsymbol{0} \\ \delta\tilde{\underline{u}}_x \\ \tilde{\boldsymbol{u}}_{2nof} \end{bmatrix} = \begin{bmatrix} \tilde{\boldsymbol{f}}_{2f} \\ \boldsymbol{0} \end{bmatrix} \tag{50}$$

where $\underline{\boldsymbol{c}}\delta\underline{\tilde{u}}_x = [\mathbf{0} \quad \delta\underline{\tilde{u}}_x]^T$ holds. Matrices $\boldsymbol{K}_{22}^{'}$, $\boldsymbol{K}_{32}^{'}$ and vectors $\boldsymbol{k}_{22}$, $\boldsymbol{k}_{32}$ are:

$$\boldsymbol{K}_{22}^{'} = \begin{bmatrix} (K_{22})_{11} & (K_{22})_{12} & \cdots & (K_{22})_{1M-1} \\ (K_{22})_{21} & (K_{22})_{22} & \cdots & (K_{22})_{2M-1} \\ \vdots & \vdots & \cdots & \vdots \\ (K_{22})_{M1} & (K_{22})_{M2} & \cdots & (K_{22})_{MM-1} \end{bmatrix} \tag{51}$$

$$\boldsymbol{K}_{32}^{'} = \begin{bmatrix} (K_{32})_{11} & (K_{32})_{12} & \cdots & (K_{32})_{1M-1} \\ (K_{32})_{21} & (K_{32})_{22} & \cdots & (K_{32})_{2M-1} \\ \vdots & \vdots & \cdots & \vdots \\ (K_{32})_{N1} & (K_{32})_{N2} & \cdots & (K_{32})_{NM-1} \end{bmatrix} \tag{52}$$

$$\boldsymbol{k}_{22} = \begin{bmatrix} \sum_{i=1}^{M}(K_{22})_{1i} \\ \sum_{i=1}^{M}(K_{22})_{2i} \\ \vdots \\ \sum_{i=1}^{M}(K_{22})_{Mi} \end{bmatrix}, \quad \boldsymbol{k}_{32} = \begin{bmatrix} \sum_{i=1}^{N}(K_{32})_{1i} \\ \sum_{i=1}^{N}(K_{32})_{2i} \\ \vdots \\ \sum_{i=1}^{N}(K_{32})_{Ni} \end{bmatrix} \tag{53}$$

Rearranging the place the known variables on the right side and unknowns to the left, gives:

$$\begin{bmatrix} -\boldsymbol{T}^{-1}\boldsymbol{K}_{22}^{-1} & -\boldsymbol{T}^{-1}\boldsymbol{K}_{22}^{-1}\boldsymbol{K}_{23} \\ -\boldsymbol{K}_{32}\boldsymbol{T}\boldsymbol{K}_{22}^{-1} & \boldsymbol{K}_{32}\boldsymbol{T}\boldsymbol{K}_{22}^{-1}\boldsymbol{K}_{32} + \boldsymbol{K}_{33} \end{bmatrix} \begin{bmatrix} \tilde{\boldsymbol{f}}_{2f} \\ \tilde{\boldsymbol{u}}_{2nof} \end{bmatrix} = \begin{bmatrix} \underline{\boldsymbol{c}}\delta\underline{\tilde{u}}_x \\ \mathbf{0} \end{bmatrix} \tag{54}$$

Now the possible bifurcations in Eq. (54) are discussed. By performing an eigenvalue analysis of the tangent stiffness matrix and obtaining the eigenvector corresponding to the zero eigenvalue, the following relationships are established:

$$\boldsymbol{\phi}_c \cdot \begin{bmatrix} \underline{\boldsymbol{c}}\delta\underline{\tilde{u}}_x \\ \mathbf{0} \end{bmatrix} = 0 \quad \Rightarrow \quad \begin{bmatrix} \underline{\boldsymbol{c}}\delta\underline{\tilde{u}}_x \\ \mathbf{0} \end{bmatrix} = \sum_{i=2}^{M+N} q_i\phi_i \tag{55}$$

or

$$\boldsymbol{\phi}_c \cdot \begin{bmatrix} \underline{\boldsymbol{c}}\delta\underline{\tilde{u}}_x \\ \mathbf{0} \end{bmatrix} \neq 0 \quad \Rightarrow \quad \begin{bmatrix} \underline{\boldsymbol{c}}\delta\underline{\tilde{u}}_x \\ \mathbf{0} \end{bmatrix} = \sum_{i=1}^{M+N} q_i\phi_i \tag{56}$$

According to asymptotic theory, the former is the bifurcation point and the latter is the limit point. The bifurcation point of the former is considered first. The linear equations are:

$$\begin{bmatrix} -\boldsymbol{T}^{-1}\boldsymbol{K}_{22}^{-1} & -\boldsymbol{T}^{-1}\boldsymbol{K}_{22}^{-1}\boldsymbol{K}_{23} \\ -\boldsymbol{K}_{32}\boldsymbol{T}\boldsymbol{K}_{22}^{-1} & \boldsymbol{K}_{32}\boldsymbol{T}\boldsymbol{K}_{22}^{-1}\boldsymbol{K}_{32} + \boldsymbol{K}_{33} \end{bmatrix} \left(\sum_{i=2}^{N+M} q_i\phi_i \right) = \sum_{i=2}^{N+M} \lambda_i q_i \phi_i \tag{57}$$

To satisfy this relation, the eigenvector corresponding to the zero eigenvalue is not needed. At the bifurcation point, deformation occurs along the direction of the zero eigenvector without any increment in δu_x. Now the limit point is considered:

$$\begin{bmatrix} -\boldsymbol{T}^{-1}\boldsymbol{K}_{22}^{-1} & -\boldsymbol{T}^{-1}\boldsymbol{K}_{22}^{-1}\boldsymbol{K}_{23} \\ -\boldsymbol{K}_{32}\boldsymbol{T}\boldsymbol{K}_{22}^{-1} & \boldsymbol{K}_{32}\boldsymbol{T}\boldsymbol{K}_{22}^{-1}\boldsymbol{K}_{32} + \boldsymbol{K}_{33} \end{bmatrix} \left(\sum_{i=1}^{N+M} q_i\phi_i \right) = \sum_{i=1}^{N+M} \lambda_i q_i \phi_i \tag{58}$$

In this case the eigenvector corresponding to the zero eigenvalue is needed. When a bifurcation occurs with a finite change in δu_x, the bifurcation mode corresponding to the zero eigenvalue eigenvector does appear.

Then the generalized coordinates are:

$$\begin{bmatrix} \delta\underline{\tilde{u}}_x \\ \tilde{\boldsymbol{u}}_{2nof} \end{bmatrix} \tag{59}$$

In order to determine the generalized force, Eq. (50) is rearranged.

$$\begin{bmatrix} \boldsymbol{K}_{22}^{'} & \boldsymbol{k}_{22} \end{bmatrix} \begin{bmatrix} \mathbf{0} \\ \delta\underline{\tilde{u}}_x \end{bmatrix} + \boldsymbol{K}_{23}\tilde{\boldsymbol{u}}_{2nof} = \tilde{\boldsymbol{f}}_{2f} \tag{60}$$

$$\delta\underline{\tilde{u}}_x \boldsymbol{k}_{22} + \boldsymbol{K}_{23}\tilde{\boldsymbol{u}}_{2nof} = \tilde{\boldsymbol{f}}_{2f} \tag{61}$$

The following equations are obtained by summing up the components in the above equation as:

$$\sum_{i=1}^{M}\sum_{j=1}^{M}(K_{22})_{ij}\delta\tilde{\underline{u}}_x + \left[\begin{array}{cccc}\sum_{i=1}^{M}(K_{23})_{i1} & \sum_{i=1}^{M}(K_{23})_{i2} & \cdots & \sum_{i=1}^{M}(K_{23})_{iN}\end{array}\right]\left[\begin{array}{c}\tilde{u}_{2nof1}\\ \tilde{u}_{2nof2}\\ \vdots \\ \tilde{u}_{2nofN}\end{array}\right] = \sum_{i=1}^{M}(\tilde{f}_{2f})_i \tag{62}$$

$$k_{22}\delta\tilde{\underline{u}}_x + \boldsymbol{k}_{23}^T\tilde{\boldsymbol{u}}_{2nof} = \tilde{f} \tag{63}$$

where the load parameter $\tilde{f}$ is defined as:

$$\tilde{f} = \sum_{i=1}^{M}(\tilde{f}_{2f})_i \tag{64}$$

Using Eq. (63), Eq. (50) is written as:

$$\left[\begin{array}{cc}k_{22} & \boldsymbol{k}_{32}^T\\ \boldsymbol{k}_{32} & \boldsymbol{K}_{33}\end{array}\right]\left[\begin{array}{c}\delta\tilde{\underline{u}}_x\\ \tilde{\boldsymbol{u}}_{2nof}\end{array}\right] = \left[\begin{array}{c}\tilde{f}\\ \boldsymbol{0}\end{array}\right] \tag{65}$$

By transferring the known variables to the right side and the unknowns to the left, the following holds:

$$\left[\begin{array}{cc}k_{22}^{-1} & -k_{22}^{-1}\boldsymbol{k}_{32}^T\\ -k_{22}^{-1}\boldsymbol{k}_{32} & k_{22}^{-1}\boldsymbol{k}_{32}\boldsymbol{k}_{32}^T + \boldsymbol{K}_{33}\end{array}\right]\left[\begin{array}{c}\tilde{f}\\ \tilde{\boldsymbol{u}}_{2nof}\end{array}\right] = \left[\begin{array}{c}\delta\tilde{\underline{u}}_x\\ \boldsymbol{0}\end{array}\right] \tag{66}$$

The tangent stiffness matrix is obtained, which corresponds to the case of imposed displacement as:

$$\left[\begin{array}{cc}k_{22}^{-1} & -k_{22}^{-1}\boldsymbol{k}_{32}^T\\ -k_{22}^{-1}\boldsymbol{k}_{32} & k_{22}^{-1}\boldsymbol{k}_{32}\boldsymbol{k}_{32}^T + \boldsymbol{K}_{33}\end{array}\right] \tag{67}$$

Extracting some parts of Eq. (54) led to Eq. (66). As with Eq. (54), if $\boldsymbol{\phi}_c$ is the eigenvector corresponding to the zero eigenvalue of the tangent stiffness matrix, the the following relation is

considered with the vector on the right side in Eq. (66).

$$\boldsymbol{\phi}_c \cdot \begin{bmatrix} \delta\tilde{\underline{u}}_x \\ \mathbf{0} \end{bmatrix} = 0 \quad \Rightarrow \quad \begin{bmatrix} \delta\tilde{\underline{u}}_x \\ \mathbf{0} \end{bmatrix} = \sum_{i=2}^{M+N} q_i \phi_i \tag{68}$$

or

$$\boldsymbol{\phi}_c \cdot \begin{bmatrix} \delta\tilde{\underline{u}}_x \\ \mathbf{0} \end{bmatrix} \neq 0 \quad \Rightarrow \quad \begin{bmatrix} \delta\tilde{\underline{u}}_x \\ \mathbf{0} \end{bmatrix} = \sum_{i=1}^{M+N} q_i \phi_i \tag{69}$$

According to asymptotic theory, the former is the bifurcation point and the latter the limit point.

Again, first the bifurcation point is considered and the linear equations become

$$\begin{bmatrix} k_{22}^{-1} & -k_{22}^{-1}\boldsymbol{k}_{32}^T \\ -k_{22}^{-1}\boldsymbol{k}_{32} & k_{22}^{-1}\boldsymbol{k}_{32}\boldsymbol{k}_{32}^T + \boldsymbol{K}_{33} \end{bmatrix} \left(\sum_{i=2}^{N+M} q_i \phi_i \right) = \sum_{i=2}^{N+M} \lambda_i q_i \phi_i \tag{70}$$

To satisfy this relation, the eigenvector corresponding to the zero eigenvalue is not needed. When a bifurcation occurs without any change in δu_x, the bifurcation mode corresponding to the eigenvector of the zero eigenvalue does appear.

Considering the latter:

$$\begin{bmatrix} k_{22}^{-1} & -k_{22}^{-1}\boldsymbol{k}_{32}^T \\ -k_{22}^{-1}\boldsymbol{k}_{32} & k_{22}^{-1}\boldsymbol{k}_{32}\boldsymbol{k}_{32}^T + \boldsymbol{K}_{33} \end{bmatrix} \left(\sum_{i=1}^{N+M} q_i \phi_i \right) = \sum_{i=1}^{N+M} \lambda_i q_i \phi_i \tag{71}$$

In this case, the eigenvector must correspond to the zero eigenvalue. When a bifurcation occurs, with no change in δu_x, there is no change corresponding to the mode of the zero eigenvalue eigenvector.

This explains how to estimate the post-bifurcation path using the above tangent stiffness matrix.

D. Bifurcation path analysis method

1. Outline

According to section III B, bifurcation points are bifurcation branching points and limit points[20]. When the solution passes through a limit point, snap-through bifurcation occurs and the

equilibrium path jumps in a discontinuous manner. The branching bifurcation points are classified as the symmetric and the asymmetric bifurcation points. Symmetric and asymmetric bifurcation points generate symmetric bifurcation buckling and asymmetric bifurcation buckling, respectively. It is possible to predict the type of bifurcation structure using asymptotic theory. However, the accuracy of the prediction is reduced because the higher order terms are neglected. In the case of snap-through buckling and symmetric bifurcation buckling, the direction of the incremental displacement from the buckling point is equal to the eigenvector corresponding to a zero eigenvalue. In the case of asymmetric bifurcation buckling, displacement and load should be changed to satisfy the relation in III B 2 (ii)-a.

At bifurcation point $(\boldsymbol{u}_c, \boldsymbol{f}_c)$, the tangent stiffness matrix $\boldsymbol{K}$ has a zero eigenvalue $\lambda_c = 0$ ($\det\boldsymbol{K} = 0$) and a corresponding eigenvector $\boldsymbol{\phi}_c$. In order to determine the position of the bifurcation point, a pinpointing procedure that is similar to the method to solve the extended system described in Wriggers, et al.[13] is used. The eigenvalue analysis of the tangent stiffness matrix is performed and $(\boldsymbol{u}_c + \epsilon\boldsymbol{\phi}_c, \boldsymbol{f}_c)$ is computed. The perturbed state is in the eigenvector direction from the bifurcation point, where ϵ is an infinitesimal parameter. By assuming the perturbed state is near a post-bifurcation path, a convergence calculation, the Newton-Raphson iteration, is performed as described in Section III B. This static analysis searches for a new equilibrium point after the bifurcation. If a post-bifurcation equilibrium point cannot be found, the initial condition is changed by varying ϵ and the search for a new equilibrium point is repeated. This method, which estimates the bifurcation mode as the eigenvector and searches for the bifurcation path, is similar to the method used in Wanger and Wriggers[13]. The difference is that Wanger and Wriggers used a directional derivative of the tangent stiffness matrix for the perturbed state. The following path analysis method algorithm has the ability to track paths after symmetric and asymmetric bifurcations, whether they are stable or unstable.

2. Analysis algorithm

If there are multiple bifurcation points with multiple zero eigenvalues, an effective way to search for buckling modes is the linear combination of eigenvectors. An algorithm to search for bifurcation

solution, where the bifurcation point is a double singular point (i.e. $\boldsymbol{K}$ has two zero eigenvalues), is shown.

1. By increasing δu_x, an eigenvalue analysis of the tangent stiffness matrix $\boldsymbol{K}$ in Eq. (66) is performed.

2. Existence of the primary path is checked. For this purpose, path tracking without perturbation $\tilde{\boldsymbol{u}}$ is performed by increasing δu_x from the initial point $(\boldsymbol{u}_c,\ \boldsymbol{f}_c)$.

3. The point $(\boldsymbol{u}_c + \boldsymbol{\epsilon}^T\boldsymbol{\Phi},\ \boldsymbol{f}_c)$ is calculated where the eigenvector $\boldsymbol{\phi}_1$ and $\boldsymbol{\phi}_2$ correspond to the zero eigenvalues, $\boldsymbol{\Phi} = [\boldsymbol{\phi}_1\ \boldsymbol{\phi}_2]$, $\boldsymbol{\epsilon} = [\epsilon\cos\theta\ \epsilon\sin\theta]^T$ and $0 < \epsilon \ll 1$, $0 \leq \theta < 2\pi$. Vector $\boldsymbol{\epsilon}^T\boldsymbol{\Phi}$ is called the disturbance vector. A convergence calculation for the static analysis is performed from this state to obtain a new equilibrium point. Various values of θ are tested and then ϵ is increased gradually to seek the post-bifurcation path. If the solution is obtained, the path tracking is performed by increasing δu_x from this state.

4. The point $(\boldsymbol{u} + \boldsymbol{\epsilon}^T\boldsymbol{\Phi},\ \boldsymbol{f})$ is calculated from the pre-buckling point$(\boldsymbol{u},\ \boldsymbol{f})$, where $\boldsymbol{\epsilon}$ and $\boldsymbol{\Phi}$ are defined in step 3. If a solution is obtained, the path tracking is performed by decreasing δu_x from this point.

An algorithm for a simple singular point follows the same progression but with a slight modification. In steps 3. and 4., $\boldsymbol{u}_c \pm \epsilon\boldsymbol{\phi}$ is used instead of $\boldsymbol{u}_c + \boldsymbol{\epsilon}^T\boldsymbol{\Phi}$ where $\boldsymbol{\phi}$ is the eigenvector of the zero eigenvalue and ϵ is an infinitesimal parameter.

IV. Analysis methods of solution

A. Symmetric solutions

Based on group theory[21], the equivalence of a system that possesses symmetry is described as:

$$\boldsymbol{M}(\gamma)\boldsymbol{f}(\boldsymbol{u}(\boldsymbol{x}),\mu) = \boldsymbol{f}(\boldsymbol{M}(\gamma)\boldsymbol{u}(\boldsymbol{M}(\gamma)\boldsymbol{x}),\mu) \tag{72}$$

The observed membrane has symmetry that is invariant with respect to e, s, r and sr, where e is the identity transformation, s is the reflection transformation with respect to xy-plane, r is the rotation

transformation by 180° about the z-axis and sr is the combination of s and r. This symmetry group is known as the dihedral group $D_2 = \{e, r, s, sr\}$. The representation matrices for the elements are:

$$\boldsymbol{M}(e) = \begin{bmatrix} 1 & 0 & 0 \\ 0 & 1 & 0 \\ 0 & 0 & 1 \end{bmatrix}, \qquad \boldsymbol{M}(r) = \begin{bmatrix} -1 & 0 & 0 \\ 0 & -1 & 0 \\ 0 & 0 & 1 \end{bmatrix}$$
$$\boldsymbol{M}(s) = \begin{bmatrix} 1 & 0 & 0 \\ 0 & 1 & 0 \\ 0 & 0 & -1 \end{bmatrix}, \qquad \boldsymbol{M}(sr) = \begin{bmatrix} -1 & 0 & 0 \\ 0 & -1 & 0 \\ 0 & 0 & -1 \end{bmatrix} \tag{73}$$

The rotation transformation is a 180° rotation about z-axis at the origin in Fig. 1. Substituting them into the governing equations (4) yields:

$$\boldsymbol{f}(\boldsymbol{M}(r)\boldsymbol{u}(\boldsymbol{M}(r)\boldsymbol{x})) = [-f_x, -f_y, f_z]^T = \boldsymbol{M}(r)\boldsymbol{f}(\boldsymbol{u}(\boldsymbol{x})) = \boldsymbol{0} \tag{74}$$

$$\boldsymbol{f}(\boldsymbol{M}(s)\boldsymbol{u}(\boldsymbol{M}(s)\boldsymbol{x})) = [f_x, f_y, -f_z]^T = \boldsymbol{M}(s)\boldsymbol{f}(\boldsymbol{u}(\boldsymbol{x})) = \boldsymbol{0} \tag{75}$$

$$\boldsymbol{f}(\boldsymbol{M}(sr)\boldsymbol{u}(\boldsymbol{M}(sr)\boldsymbol{x})) = [-f_x, -f_y, -f_z]^T = \boldsymbol{M}(sr)\boldsymbol{f}(\boldsymbol{u}(\boldsymbol{x})) = \boldsymbol{0} \tag{76}$$

Hence, the symmetry transformations satisfy the equivalence condition of the governing equations. In addition, the boundary conditions in Eqs. (5) to (8) are invariant under the symmetry transformations. As a result, this system has the symmetry that is invariant under all possible transformations.

Deformation $\boldsymbol{u}_0(x, y, z)$ satisfies the governing equations (4) and boundary conditions of Eqs. (5) to (8). Three deformations $\boldsymbol{u}_s(x, y, z)$, $\boldsymbol{u}_r(x, y, z)$, and $\boldsymbol{u}_{sr}(x, y, z)$ are obtained from $\boldsymbol{u}_0(x, y, z)$ by means of the reflection transformation, the rotation transformation, and the rotation and reflection transformation, respectively. The three deformations $\boldsymbol{u}_s$, $\boldsymbol{u}_r$, and $\boldsymbol{u}_{sr}$ are the solutions satisfying the governing equations (4) and the boundary conditions of Eqs. (5) to (8).

Symmetry between two solutions is defined through an example. If deformation $\boldsymbol{u}_1(x, y, z)$ is equivalent to $\boldsymbol{u}_{sr}(x, y, z)$, there exists a symmetry where $\boldsymbol{u}_0$ agrees with $\boldsymbol{u}_1$ using the rotation and reflection transformation. Also, $\boldsymbol{u}_1$ is equivalent to $\boldsymbol{u}_0$ transformed by the rotation and reflection transformation. In other words, $\boldsymbol{u}_0$ and $\boldsymbol{u}_1$ have the rotation and reflection symmetry. The

deformation $\boldsymbol{u}_1$ is a different representation of $\boldsymbol{u}_0$.

Symmetry in a solution can also be defined through an example. If $\boldsymbol{u}_0(x,\, y,\, z)$ is equivalent to $\boldsymbol{u}_r(x,\, y,\, z)$, then $\boldsymbol{u}_0$ has the symmetry that is invariant under the rotation transformation. Also, $\boldsymbol{u}_0$ has the rotation symmetry. In this case, $\boldsymbol{u}_r$ is obtained, which is equivalent to $\boldsymbol{u}_0$ by the rotation transformation. It is said that we obtain the same solution or we do not obtain a new solution by the transformation.

B. Similarity value

In order to identify similarity between the two solutions, the similarity value is constructed as the inner product of solutions:

$$< f_1(n_x,\, n_y),\, f_2(n_x,\, n_y) >= \sum_{p=1}^{N_x} \sum_{q=1}^{N_y} \hat{f}_1(m,\, n) \hat{f}_2^*(m,\, n) \tag{77}$$

where $f_j(n_x,\, n_y)$ is a vector whose components are displacement values sampled at all finite element nodes and $\hat{f}_j(m,\, n)$ is the discrete Fourier transformation of $f_j(n_x,\, n_y)$.

The similarity value is evaluated using the first bifurcation point of the membrane. Because of membrane symmetry, the first bifurcation point is also symmetric, as is theoretically predicted. Therefore, the theoretical similarity value between two deformations should be 1. However, the above defined similarity value is based on a discrete set. When the similarity value of f_1 and f_2 are obtained numerically after the first bifurcation point, a value of 0.999995... was obtained. Therefore, the values after the fifth digit are considered to be numerical error. During comparison of different wrinkle patterns, the number of digits to which similarity is obtained is referred, e.g. 0.99999345 achieved similarity within 5 digits.

C. Bifurcation diagram

A method of expressing the equilibrium path as it passes through the bifurcation point is needed. Here, calculating the inner product of the eigenvector and the incremental displacement vector is considered to make a bifurcation diagram.

At the bifurcation point $(\boldsymbol{u}_c,\, \boldsymbol{F}_c)$, the tangent stiffness matrix $\boldsymbol{K}_c$ becomes $\det \boldsymbol{K}_c = 0$. At

this point there exist N_c zero eigenvalues $\lambda_{ci} = 0$ $(i = 1, \ldots, N_c)$ and corresponding eigenvectors $\boldsymbol{\phi}_{ci}$.

$$\boldsymbol{K}_{ci}\boldsymbol{\phi}_{ci} = \lambda_{ci}\boldsymbol{\phi}_{ci} \quad (i = 1,\, 2,\, \ldots,\, N_c)$$

where $\boldsymbol{\phi}_{ci}$ is normalized as $||\boldsymbol{\phi}_{ci}|| = 1$. Using $\lambda_{ci} = 0$ and where c_i is an arbitrary constant results in:

$$\boldsymbol{K}_c \left(\sum_{i=1}^{N_c} c_i \boldsymbol{\phi}_{ci} \right) = \mathbf{0} \tag{78}$$

As explained in the earlier section the incremental displacement $\tilde{\boldsymbol{u}}_c$ occurs whereas the incremental load $\tilde{\boldsymbol{f}} \simeq \mathbf{0}$:

$$\boldsymbol{K}_c \tilde{\boldsymbol{u}}_c \simeq \mathbf{0} \tag{79}$$

Combining Eq. (78) and Eq. (79) the following holds:

$$\tilde{\boldsymbol{u}}_c \simeq \sum_{i=1}^{N_c} c_i \boldsymbol{\phi}_{ci} \tag{80}$$

The displacement increment after the bifurcation point, $\tilde{\boldsymbol{u}}$ is expressed as a linear combination of eigenvectors $\boldsymbol{\phi}_{ci}$ corresponding to the zero eigenvalues of the tangent stiffness matrix. Calculation of c_i is as:

$$c_i = \tilde{\boldsymbol{u}}_c \cdot \boldsymbol{\phi}_{ci} \; (i = 1,\, \ldots,\, N_c) \tag{81}$$

For construction of the bifurcation diagram, c_i will be used.

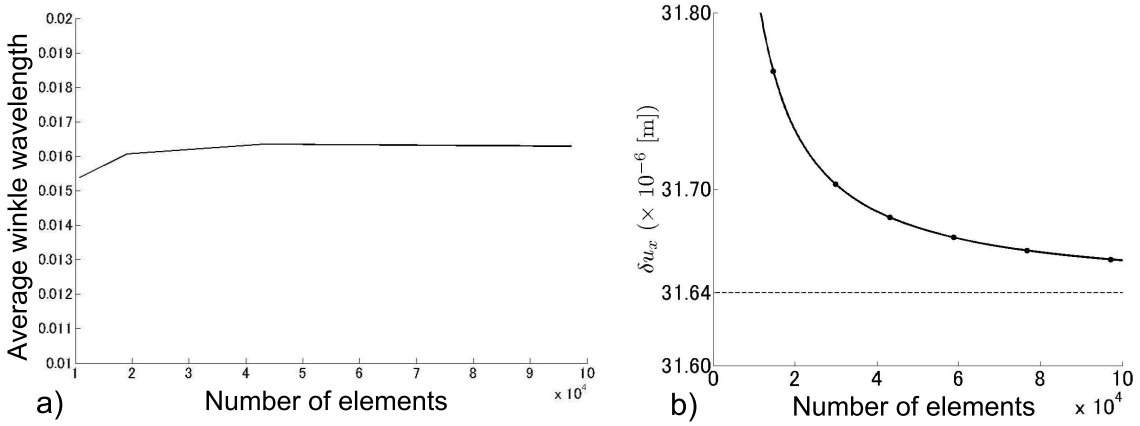

Fig. 2 Convergence: a) wrinkle wavelength with element number, and b) δu_x at the first bifurcation point with element number.

V. Numerical results

A. Validity of the FEM modeling

The geometry, properties, and boundary conditions mentioned in section II are modeled in ABAQUS. Based on discussions in Wong and Pellegrino[6], the S4R (4 node shell element with reduced Gauss integration) elements are selected. Using this element, numerical results agree best with the experimental results in Wong and Pellegrino[4] and Inoue[17]. The number of elements is $360 \times 120 = 4.23 \times 10^4$, which is the same value used in Wong and Pellegrino[6] for a membrane with an aspect ratio of 3:1. By maintaining square elements, the number of elements can be increased or decreased by changing the number of elements along a single edge of the membrane, where the other edge is determined by the aspect ratio.

By increasing the shear displacement up to $\delta u_x = 250 \times 10^{-6}$[m], the wavelength and amplitude of wrinkles are observed as indicators of wrinkle shape at at section AA'. Because of the free boundaries, the wrinkle amplitude and wavelength near those boundaries varies by a large amount. By omitting the first 6 wrinkles from each free boundary, the amplitude and wavelength average of the remaining wrinkles is closer to the individual values. Fig. 2 a) shows the convergence of wavelength with respect to the number of elements in the FE model. Thus, the element number $360 \times 120 = 4.23 \times 10^4$ achieves sufficient convergence. A larger number of elements would increase the computational cost with minimum improvements wavelength accuracy. The amplitude convergence is similar and omitted.

When compatibility and completeness conditions are satisfied, an asymptotic convergence toward the continuum model is obtained by increasing the number of elements. Considering the problem of this study, the shear displacement δu_x needed for the first bifurcation point is analyzed with respect to the mesh density. The dots in Fig. 2 b) are obtained by this analysis, and a function $y = a_1 x^{-2} + a_2 x^{-1} + a_3$ is used to connect them. The convergence indicates that the bifurcation point is located at 31.64×10^{-6} [m]. As can be seen, the FEM model with $360 \times 120 = 4.32 \times 10^4$ elements has a relative error of 0.13 %. The conclusion is that sufficient convergence has been obtained.

Models with more elements, e.g. 375×125, 390×130, and 432×144 were also used for analysis. The results from these numbers of elements were compared to the result from 360×120 elements to confirm that the results converged and were insensitive above 4.32×10^4 elements. This also applies to results for $\delta u_x > 250 \times 10^{-6}$[m].

The convergence of the numerical results is controlled by two additional parameters in the ABAQUS calculation. First, R_n^α is the convergence criterion for the ratio of the largest residual to the corresponding average flux norm. The default value is $R_n^\alpha = 5 \times 10^{-3}$. Second is C_n^α, which is the convergence criterion for the ratio of the largest solution correction to the largest corresponding incremental solution value. Its default value is $C_n^\alpha = 1 \times 10^{-2}$. For general analysis, the default values are sufficient; however, to obtain more precise results, values that are 10^{-4} times of the default values are used combined with the δu_x increment of 10^{-7}[m].

B. Membrane behavior

As defined in Section II, the imposed displacement is applied to the membrane at the top boundary and the deformation is calculated. This is done mainly through the observation of the membrane deformation and through the bifurcation structure. Stress states are observed at specific points of interest. For the deformation, the displacement value $u_z(x, y)$ in the z-direction on the mid-plane is shown in the figures. The first and second principal stresses are presented as $\sigma_\xi(x, y)$ and $\sigma_\eta(x, y)$ whose directions are coincident with $\xi\xi'$ and $\eta\eta'$, which are related to the wrinkle shape.

Displacement is imposed on the top edge, first in y-direction as $\delta u_y = 30 \times 10^{-6}$[m]. The

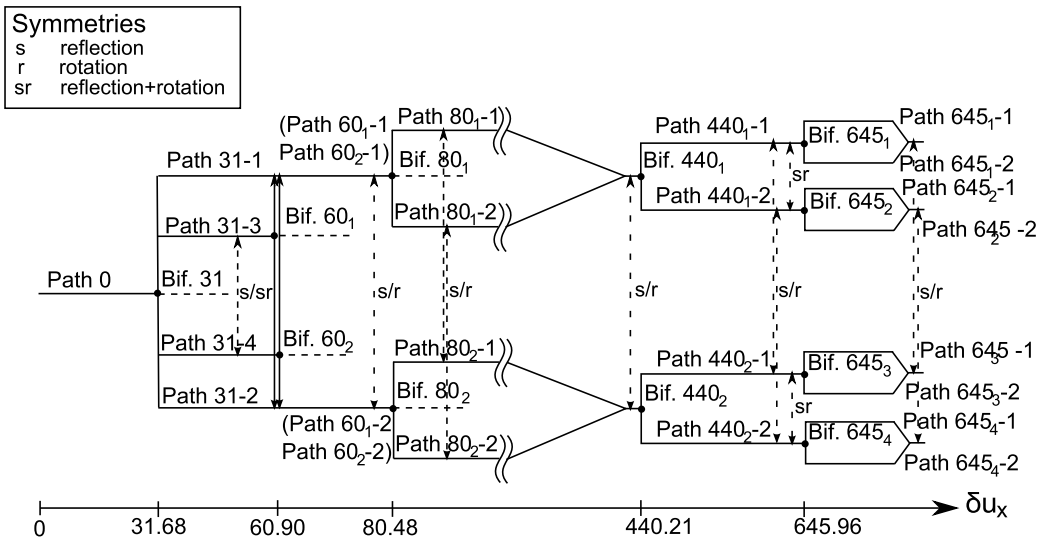

Fig. 3 Schematic bifurcation diagram with respect to imposed shear displacement δu_x.

incremental displacement in x-direction is imposed δu_x from 0[m] to 650×10^{-6}[m]. The schematic bifurcation diagram is shown in Fig. 3. This bifurcation diagram will be used to illustrate membrane behavior as δu_x is increased.

For notation, bifurcation points are indicated by 'Bif. X_n', where X indicates the micrometer value of the δu_x where the bifurcation point occurs. The subscript n is an identifier used if there are multiple bifurcation points at the same value of δu_x. Paths are indicated by 'Path Y-m', where Y is the value of the δu_x where the path starts, and m is an identifier if there are multiple paths that start at the same point.

1. Path 0

The equilibrium path is observed for the interval $0 \leq \delta u_x < 31.68 \times 10^{-6}$[m]. The initial imposed displacement is $\delta u_y = 30 \times 10^{-6}$[m] and $\delta u_x = 0$ so the membrane remains flat. This results in a tensile σ_{yy} and, because of the Poisson effect, a tensile σ_{xx}. A state of biaxial tension is maintained throughout most of the membrane. On free boundaries, $\sigma_{xx} = 0$ because no stress is applied from outside of the free boundaries. The σ_{xx} near the free boundaries is smaller than in the central region. As δu_x is increased, the out-of-plane deformation remains 0 and planar shear deformation is observed. This path is followed until $\delta u_x = 31.68 \times 10^{-6}$[m], where the first bifurcation point is detected as Bif. 31.

2. Bif. 31

At Bif. 31 of $\delta u_x = 31.68 \times 10^{-6}$[m], the single equilibrium path branches into four paths, Paths 31-1, 31-2, 31-3 and 31-4. All post-bifurcation paths contain wrinkles that are generated at this point. Bif. 31 is a double singular point with a two zero eigenvalues and its bifurcation diagrams are shown in Fig. 4. The deformations at $\delta u_x = 31.83 \times 10^{-6}$[m] after Bif. 31 are shown in Fig. 5.

Using the algorithm explained in Section III D, the post-bifurcation paths are searched for using disturbance vectors for $0 < \theta \leq 2\pi$. As the imposed displacement is increased from $\delta u_x = 31.68 \times 10^{-6}$[m], every path converges on one of four paths that are detected after this point. As Fig. 4 indicates, Paths 31-1, 31-2, 31-3, and 31-4 are paths whose directions are almost same as the disturbance vectors of $\theta = \pi/4, 5\pi/4, 7\pi/4, 3\pi/4$. Figure 4 b) shows the proximity of the bifurcation point in more detail. Because this is a double singular bifurcation point, it has stable paths for any $0 < \theta \leq 2\pi$ as indicated by the stable surface. As shear displacement is increased, the surface is reduced to one of the four paths leading away from the point.

The out-of-plane deformations of these four paths are shown in Fig. 5. By observing the wrinkles closest to the free boundary, the side with an upward convex wrinkle is identified by + and the side with a downward convex wrinkle by −. The wrinkle patterns of four paths are then indicated as follows: Path 31-1 as (+, −), Path 31-2 as (−, +), Path 31-3 as (−, −), and Path 31-4 as (+, +).

Relative to the rest of the membrane, the center of the membrane remains flat. A single wrinkle pattern that occupies half of the membrane can be identified. By applying the rotation transformation, the reflection transformation and the rotation and reflection transformation to this one wrinkle pattern occupying half of the membrane and combining the transformations, all full membrane wrinkle patterns are obtained. Because of this symmetry, one wrinkle pattern exists on each side, and has + or − sign. This symmetry also results in four wrinkle patterns for the whole membrane. Paths 31-1 and 31-2 are equivalent with both the reflection transformation about xy-plane and the rotation transformation. The same applies to Paths 31-3 and 31-4. Thus these paths appear symmetric in the bifurcation diagram.

Figure 6 a) and b) shows the first principal stress σ_ξ and second principal stress σ_η at the mid-plane. The initial position of wrinkles near the free boundaries is explained by the compressive

stress σ_η near the free boundaries. Therefore, wrinkle formation is expected.

Similarly to Path 0, σ_{xx} near the free boundaries is smaller. As δu_x is increased, the tensile stress to the right and upper direction increases, and σ_ξ becomes as shown in Fig. 6 a) and σ_η becomes as shown in Fig. 6 b). Therefore, the region near the free boundaries takes on the states of uniaxial compression, whereas the other region is in biaxial tension. As δu_x is increased, the compressive regions near the boundaries expand toward the middle, and their compression amplitudes increase.

3. Path 31

By increasing δu_x until $\delta u_x = 60.90 \times 10^{-6}$[m], all four paths connected from Bif. 31 are observed. The behavior on this path is represented by the generation of new wrinkles one after another on the flat part of the membrane next to existing wrinkles.

This process is shown for Path 31-3 in Fig. 7. Similar behavior occurs along all other paths. A small wrinkle is generated next to existing wrinkles on each side of the flat part of the membrane. By increasing δu_x, this wrinkle grows until it makes contact with the top and bottom boundaries. Once both contacts have been made, the rest of the membrane, up to the middle area, changes its sign in the z-direction, but remains flat. This is followed by the generation of a new wrinkle on each side.

This process is repeated until the flat section of the membrane is filled with wrinkles. Additional shear will increase the number of wrinkles and the amplitude of the wrinkles. The process can be observed for the AA' cross-section in Fig. 8 b). The process for Path 31-1 is shown in Fig. 8 a) The other two paths have reflection symmetry behavior, and are omitted. This behavior will be discussed in more detail in a later section.

In Fig. 9 the out-of-plane deformation at $\delta u_x = 60.00 \times 10^{-6}$[m] is shown, just before the upcoming bifurcation. Here, Paths 31-1 and 31-2 have 34 wrinkles and Paths 31-3 and 31-4 have 33 wrinkles. The four paths keep their wrinkle patterns as follows. Paths 31-1, 31-2, 31-3, and 31-4 are identified as (+, −), (−, +), (−, −), and (+, +), respectively.

The key point is that during this process, the eigenvalue analysis of the tangent stiffness matrix showed that all eigenvalues remain positive. Therefore, this wrinkle generation is not a result of

bifurcation behavior. This wrinkle generation mechanism is regarded as unique. How this is achieved will be shown in a later section.

4. Bif. 60

The second bifurcations on this membrane are Bif. 60_1 and Bif. 60_2 at $\delta u_x = 60.90 \times 10^{-6}$[m] on Path 31-3 and Path 31-4, respectively. For Path 31-1 and Path 31-2, all eigenvalues of the tangent stiffness matrix remain positive at larger values of δu_x. At this point, wrinkle generation without bifurcation is complete. No flat sections remain on the membrane.

For Path 31-3, a snap through bifurcation is observed, where one zero eigenvalue is obtained at $\delta u_x = 60.90 \times 10^{-6}$[m], and the path jumps to either Path 60_1-1 or 60_1-2. A change in sign occurs near the right free boundary, and it results in a $(-, -)$ configuration becoming a $(+, -)$ configuration. Similarly, when the jump is to Path 60_1-2, the change is on the right side from $(-, -)$ to $(-, +)$. This transition is the rotational symmetry of the former. Symmetrical transitions occur along Path 31-4. The transition for Path 31-4 with $(+, +)$ to Path 60_2-2 with $(+, -)$ is the reflection symmetry of the first transition. The transition from Path 31-4 with $(+, +)$ to Path 60_2-1 with $(-, +)$ is the rotation and reflection symmetry of the first transition.

The comparison of the deformation on Path 60_1-1 and Path 31-1 at $\delta u_x = 61.00 \times 10^{-6}$ results in 7 digit similarity using the similarity value in section IV. Therefore, Path 60_1-1 and Path 60_2-1 are equivalent to Path 31-1. Also, Path 60_1-2 and Path 60_2-2 are equivalent to Path 31-2.

The bifurcation structure for this point is shown in Fig. 10 a). By increasing δu_x, the main path ($c_1 = 0$) becomes unstable at $\delta u_x = 60.90 \times 10^{-6}$[m]. The system then follows either Path 60_1-1 or 60_1-2 that is Path 31-1 or 31-2. Path 31-1 or 31-2 are symmetrically positioned at $c_1 = \pm 1.05 \times 10^{-4}$. This is considered as a symmetric snap through bifurcation. If δu_x is decreased from values larger than $\delta u_x = 60.90 \times 10^{-6}$[m], the system on Paths 60_1-1 and 60_1-2 will not go back to the primary path of Path 31-3. The system follows Paths 31-1 and 31-2 back to Bif. 31. This bifurcation structure and its behavior are the same for both Path 31-3 and Path 31-4.

The conclusion is that after $\delta u_x = 60.90 \times 10^{-6}$[m], there are only two stable equilibrium paths corresponding to Paths 31-1 and 31-2. Their wrinkle configurations are almost the same as shown

in Fig. 9 a) and b).

5. Path 60

Paths 60_1-1 and 60_2-1 are equivalent to Path 31-1 on the interval $60.90 \times 10^{-6} \leq \delta u_x < 80.48 \times 10^{-6}$[m]. Similarly, Paths 60_1-2 and 60_2-2 are equivalent to Path 31-2 on the same interval. For the paths on this interval, the increase in δu_x results in only a wrinkle amplitude increase. Wrinkle patterns are preserved.

6. Bif. 80

Following the two Paths 31-1 and 31-2, which remain after $\delta u_x = 60.90 \times 10^{-6}$[m], bifurcation points Bif. 80_1 and Bif. 80_2 occur at $\delta u_x = 80.48 \times 10^{-6}$[m].

For Path 31-1 at Bif. 80_1, the occurrence of a zero eigenvalue leads to a deformation of wrinkles in the middle section ($-0.05 < x < 0.05$[m]) of the membrane. The bifurcation results in two wrinkle patterns, as shown in Fig. 11 a) and b) that are Paths 80_1-1 and 80_1-2. They are similar to each other, but result in only 3 digits of similarity. Deformation is represented by a local drop in wrinkle amplitude near the fixed boundaries on both top and bottom edges of the membrane. Section $\xi\xi'$ of the wrinkles is positioned as in Fig. 1, on Path 80-1. The amplitude decrease occurs along an upward convex wrinkle on the right side (positive direction of x) of section $\xi\xi'$ and along a downward convex wrinkle on the left side of section $\xi\xi'$. The symmetric deformation occurs on Path 80-2. The drop in amplitude occurs along an upward convex wrinkle to the left side (negative direction of x) and along a downward convex wrinkle on the right side of section $\xi\xi'$. In Fig. 11 c), a comparison of the two wrinkle patterns is defined as $(u_z(x,y))_{Path\ 80-1} - (u_z(x,y))_{Path\ 80-2}$ and the difference is observed.

For Path 31-1 at Bif. 80_1, the bifurcation diagram is shown in Fig. 10 b). This is a simple bifurcation point with one zero eigenvalue. A snap-through bifurcation occurs where Path 31-1 jumps to Path 80_1-1 or Path 80_1-2. The disturbance vectors, i.e. the imposed eigenvectors to search for the post-bifurcation paths, are symmetric in reflection. However, when the entire wrinkle pattern is considered, Paths 80_1-1 and 80_1-2 are not equivalent to any of the three symmetry transformations, i.e. the reflection, the rotation, and the reflection and rotation transformations. Therefore, path

tracking along both paths is needed.

Paths 31-1 and 31-2 are equivalent by the reflection or the rotation transformations. Hence, the behavior at Bif. 80_2 on Path 31-2 is similar to the behavior of Bif. 80_1 mentioned above. Also, the resulting Paths 80_2-1 and 80_2-2 are not equivalent by any of the three symmetry transformations.

The deformations on Paths 80_1-1 and 80_2-1 are equivalent by the reflection or the rotation transformations. The deformations on Paths 80_1-2 and 80_2-2 are also equivalent by the reflection or the rotation transformations.

7. Path 80

Path tracing continues on the interval $80.48 \times 10^{-6} \leq \delta u_x < 440.21 \times 10^{-6}$[m] following Path 80_1-1 and Path 80_1-2.

The behavior along these paths is represented by the generation of local wrinkles near the top and bottom edges, one after another. This process along Path 80_1-1 is shown in Fig. 12. When δu_x is increased, the wrinkle amplitude decreases locally near the fixed boundaries, leading to curvature inflections. This characteristic formation is referred to as a collapsed section. As δu_x is increased, the decrease in amplitude will eventually result in a wrinkle section with an amplitude of 0, which then starts to increase to the opposite sign of the rest of the wrinkle.

With increasing δu_x, these collapsed sections will grow in size. In addition, these sections will also shift their positions. What is observed is that both amplitude change and position shifts occur while all eigenvalues of the tangent stiffness matrix remain positive. At $\delta u_x = 440.00 \times 10^{-6}$[m] in Fig. 13 a) and b), most central wrinkles have collapsed sections.

The behavior on Path 80_1-2 is similar to Path 80_1-1. Again, a comparison of $(u_z(x,y))_{Path\ 80-1} - (u_z(x,y))_{Path\ 80-2}$ is shown in Fig. 13 c). The similarity value defined in Section IV determines that the paths are similar to within five digits without any transformation. In conclusion, as both paths experience position shifts of collapsed sections, they both converge to a single wrinkle pattern.

The other two paths, Paths 80_2-1 and 80_2-2, are equivalent to Paths 80_1-1 and 80_1-2 by the reflection or the rotation transformations.

8. Bif. 440

Path tracking of both Path 80_1-1 and 80_1-2 determines the next bifurcation point at $\delta u_x = 440.21 \times 10^{-6}$[m] as Bif. 440_1. It is a simple singular point and the path branches to either Path 440_1-1 or 440_1-2.

Along Paths 80_1-1 and 80_1-2, collapsed sections increase in size. At $\delta u_x = 440.21 \times 10^{-6}$[m], the collapsed sections of two wrinkles reach critical sizes. One of the wrinkles will split into new wrinkles.

In Fig. 14, the behavior at this point can be observed. The wrinkle pattern at $\delta u_x = 440.21 \times 10^{-6}$[m], before the disturbance vector imposition, is shown in Fig. 14 a). The disturbance vector imposition causes a snap through bifurcation. The above pattern jumps to one of the patterns observed in Fig. 14 b) and c). The collapsed sections near the top and bottom fixed boundaries of one wrinkle expand toward the middle of the wrinkle. By increasing shear to $\delta u_x = 440.50 \times 10^{-6}$[m], the generation of new wrinkles is finalized as in Fig. 14 d) and e). The expanded collapsed sections meet, and the wrinkle amplitude along the center drops until it changes its sign. One wrinkle generates two new wrinkles, one of the same sign and one with the opposite sign.

Comparing the two wrinkle patterns on Paths 440_1-1 and 440_1-2, one is the equivalent of the other by the rotation and reflection transformation. Similarity up to five digits is calculated. Because the two paths are symmetric, only one is tracked until the next bifurcation.

The above behavior and the behavior at Bif. 440_2 on Paths 80_2-1 and 80_2-2 have either reflection or rotation symmetry.

9. Path 440

Path 440_1-1 is tracked along the interval $440.21 \times 10^{-6} \leq \delta u_x < 645.96 \times 10^{-6}$[m].

Bif. 440_1 results in single wrinkle collapsed sections merging and generating new wrinkles. Collapsed sections on other wrinkles remain. The behavior on Path 440_1-1 is similar to that of Path 80, where existing collapsed sections grow and shift in position.

Behavior of Path 440_1-2 is equivalent to Path 440_1-1 by the rotation and reflection transformation. The above paths, Paths 440_1-1 and 440_1-2, and the other two paths, Paths 440_2-1 and 440_2-2,

have reflection or rotation symmetry.

10. Bif. 645

The next bifurcation point on Path 440_1-1 is Bif. 645_1 at $\delta u_x = 645.96 \times 10^{-6}$[m]. It is a simple singular point and the path branches to either Path 645_1-1 or 645_1-2.

Collapsed sections of two wrinkles reach a critical size. One splits into new wrinkles. The wrinkle pattern at $\delta u_x = 645.96 \times 10^{-6}$[m], before the disturbance vector imposition, is shown in Fig. 15 a). Collapsed sections near the top and bottom fixed boundaries expand toward the middle of the wrinkle as in Fig. 15 b) and c). A slight increase in shear to $\delta u_x = 646.00 \times 10^{-6}$[m] completes the wrinkle generation, see Fig. 15 d) and e). The process is the same as in Bif. 440_1.

By comparing the two wrinkle patterns representing Paths 645_1-1 and 645_1-2 at $\delta u_x = 647.00 \times 10^{-6}$[m], a five digit similarity without any transformations is determined. Therefore, a single path can be considered after this bifurcation point.

The behavior at Bif. 645_2 on Path 440_1-2 is equivalent to Bif. 645_1 transformed by the rotation and reflection transformation.

The behaviors at Bif. 645_3 and Bif. 645_4 are equivalent to Bif. 645_1 and Bif. 645_2 after transformation by the reflection or the rotation transformations.

C. Wrinkle generation without bifurcations

In the previous sections, observed results for the membrane behavior were shown. These results showed bifurcation points and wrinkle patterns for a range of imposed displacement at $0 \leq \delta u_x \leq 650 \times 10^{-6}$[m]. Now, the focus is on the wrinkles generated without bifurcations. This wrinkle generation occurs on equilibrium paths between the first and second bifurcation point. Therefore, it is not related to bifurcation points. The behavior is calculated by the path tracking analysis.

1. Observations

Bifurcation free wrinkle generation is observed in the interval of imposed displacement of $31.68 \times 10^{-6} < \delta u_x \leq 60.90 \times 10^{-6}$[m]. As δu_x is increased, the number of wrinkles increases along all four paths originating from Bif. 31. Along the interval, every path is stable, i.e. the tangent stiffness

matrix $\boldsymbol{K}$ on every path is positive definite, and wrinkle generation occurs at stable equilibrium points.

The process of wrinkle generation for a single wrinkle on Path 31-3 is shown in Fig. 7. Figure 7 a) shows the wrinkle pattern at $\delta u_x = 35.00 \times 10^{-6}$[m]. Near the free boundaries, there are three upward convex and three downward convex wrinkles along each boundary. The middle of the membrane remains flat. In Fig. 7 b), the imposed displacement is increased to $\delta u_x = 36.00 \times 10^{-6}$[m]. A small wrinkle is generated on the flat surface of the membrane, next to existing wrinkles. This wrinkle does not stretch from the top to bottom edges of the membrane. In Fig. 7 c) imposed displacement is increased further to $\delta u_x = 37.00 \times 10^{-6}$[m]. The new wrinkle on the right side expands to the top boundary. The wrinkle on left side expands to the bottom boundary. By further increasing the imposed displacement to $\delta u_x = 38.00 \times 10^{-6}$[m], a new wrinkle pattern, shown in Fig. 7 d) emerges. Now, the new small wrinkles run from top to bottom. Once the small wrinkles expand from top to bottom, the middle of the membrane changes sign in z-direction. However, the middle remains flat. In this process, where new wrinkles are generated, three new upward convex and four new downward convex wrinkles are observed on each side.

In Figs. 6 c) and d), the two-dimensional stress state on the mid-plane is shown for $\delta u_x = 38.00 \times 10^{-6}$[m]. The first principal stress σ_ξ is tensile throughout the membrane. The second principal stress σ_η is tensile in the middle, on the flat part of the membrane, while it is compressive around the wrinkled areas. However, the compressive stress area does not cover the small wrinkles in Fig. 7 b). Because these small wrinkles are under biaxial tension, to distinguish them from other wrinkles, they are referred to as waves. Wrinkles occur as a result of buckling in a compressive stress area. Waves are generated without buckling in a biaxial tension stress area. The first axis tension and second axis compression area is referred to as the compressive stress areas.

One by one, waves are generated on each side of the flat section of the membrane. As imposed displacement δu_x increases, the compressive stress area expands toward the middle of the membrane. When the compressive stress area covers the wave, by definition the wave becomes a wrinkle. Therefore, a wrinkle is generated without bifurcation buckling.

To show the process in more detail, section CD in the $\eta\eta'$ direction is constructed as shown

in Fig. 6 e). The position in section CD is defined by node numbers, projections of finite element nodes onto section CD. The total number of nodes is 30. Figure 16 shows the results for $\delta u_x = 37.58 \times 10^{-6}$[m], $\delta u_x = 37.75 \times 10^{-6}$[m], $\delta u_x = 38.00 \times 10^{-6}$[m], and $\delta u_x = 38.20 \times 10^{-6}$[m]. Depending on the behavior, each figure illustrates an appropriate node range.

Figure 16 d) shows the second principal stress σ_η in section CD. The compressive stress area progresses into the middle. It also shows that there are both the compressive stress area and the biaxial tensile stress areas in section CD. The second principal stress at every node decreases as δu_x increases. Figure 16 e) shows the minimal principal stress in the node interval from 10 to 14 in section CD. The border between the positive and the negative second principal stress areas moves from node 11 to 13 toward point D when the imposed displacement increase from $\delta u_x = 37.58 \times 10^{-6}$[m] to $\delta u_x = 38.20 \times 10^{-6}$[m]. The key point is that the area of node 13 and its right side is the biaxial tensile stress area by $\delta u_x = 38.20 \times 10^{-6}$[m].

Figure 16 a) shows an increase of out-of-plane displacement between nodes 1 and 11 as δu_x is increased. Figure 16 b) shows the out-of-plane displacement more closely between nodes 12 and 19. As the imposed displacement δu_x is increased, the out-of-plane displacement decreases between nodes 14 and 16.

Figure 16 c) shows a change in curvature from positive to negative between nodes 15 and 20 at $\delta u_x = 38.00 \times 10^{-6}$[m]. At $\delta u_x = 38.20 \times 10^{-6}$[m], the wave is convex upward. Recalling Fig. 16 d), the area after node 13 is a biaxial tensile stress area. Therefore, this is not a wrinkle but a wave.

2. Wrinkle generation mechanism

Increasing the imposed displacement δu_x from 0, the semicircular regions of uniaxial compression near the free boundaries occur, while the other region remains as a biaxial tension stress area, as indicated by Fig. 6 d). The compressive stress regions gradually expand toward the middle of the membrane with increasing δu_x. This is confirmed by Fig. 16 d).

For the path segment of interest, $37.58 \times 10^{-6} \leq \delta u_x \leq 38.20 \times 10^{-6}$[m], the middle section of the membrane including point D tends to remain flat without out-of-plane displacement due to biaxial tension.

Figure 16 a) shows that there is a downward convex wrinkle near node 3 and an upward convex wrinkle near node 8. Their curvature magnitudes are large. The region from node 1 to node 11 is always a compressive stress area, but its second principal stress σ_η decreases toward node 11. Combining the large curvatures and the decreasing second principal stress results in larger out-of-plane displacements, see the variation between node 1 and 11 in Fig. 16 a).

The out-of-plane displacements of the wrinkles near the free boundary converge to zero toward point D. In Fig. 16 b), while the out-of-plane displacement around node 12 increases, the out-of-plane displacement around node 14 decreases. For this process, the bending moment M_ξ is given in Fig. 16 f) and g) and the section transversal force N_z is given in Fig. 16 h). The bending moment and the transversal force are applied to the membrane due to the existence of bending rigidity in the model.

The bending moment changes from positive to negative around node 14. It reaches the minimum value around node 15, and it converges to 0 toward the middle of the membrane. By increasing δu_x, the minimum value also decreases. This negative value of the bending moment results in a downward convex deformation of the membrane.

The transverse force N_z is negative between nodes 8 and 15. This means a downward force is applied in the region. The peak of an upward convex wrinkle occurs near node 8. On this wrinkle, the larger tensile stress σ_ξ and the curvature along ξ causes a negative transverse force. The smaller compressive stress σ_η and the curvature along η cause a smaller positive transverse force. These result in a negative transverse force near node 8. This is confirmed by the fact that a positive transverse force, i.e. an upward force, is applied to a downward convex wrinkle near node 3.

As a result, in Fig. 16 b) the deformation is convex upward until node 14, but it becomes convex downward at node 15. In addition, the left side of node 15 is pushed downward. At $\delta u_x = 38.00 \times 10^{-6}$[m], this results in a small region of negative curvature between node 15 to 20. As this region is under biaxial tension, the deformation with varying curvature is a wave.

In summary, initial wrinkles exist in a uniaxial compression region. The biaxial tension region is generally flat. In the biaxial tension region near the existing wrinkles, a wave deformation is generated. This phenomena can be considered as the origin of wrinkles. As the imposed displacement

δu_x is increased, the uniaxial compression region spreads to the wave and transforms it into a wrinkle. This process occurs without bifurcations. As the uniaxial compression region spreads, the new wrinkle grows in size and generates the conditions for a new wave. The whole process repeats itself. This is a wrinkle generation mechanism without bifurcations.

VI. Conclusion

Because wrinkle generation is generally considered to be a result of bifurcations, the expected result was a branching structure at every wrinkle generation. This could potentially result in a large number of equilibrium paths where each represents a specific wrinkle pattern. However, as the results show, significantly fewer equilibrium paths were obtained. This was due to wrinkle generation without bifurcation and to deformation symmetry.

The first bifurcation generates the initial wrinkles along four equilibrium paths. The membrane is divided into the biaxial tension area and the uniaxial compression areas. Wrinkles are only generated in the uniaxial compression area. A wave is generated in the biaxial tension area, near the uniaxial compression area. With increasing shear displacement, the uniaxial compression area expands onto the wave and turns it into a wrinkle. The process of wrinkle generation without bifurcation repeats on all four paths until no section of flat membrane remains. The number of wrinkles increases to 33 and 34. This wrinkle generation without bifurcation results in fewer equilibrium paths than expected for this number of wrinkles.

Increasing shear further causes wrinkle amplitude to increase until the next bifurcation. Different behavior occurs where small sections of existing wrinkles collapsed. With further increases in shear displacement, these collapsed sections govern wrinkle generation by destabilizing existing wrinkles. This is the expected behavior for bifurcations causing wrinkle generation. However, the wrinkle patterns after wrinkle generation show symmetry, resulting in fewer unique wrinkle patterns.

Based on the results of the above analysis, the following conclusions can be made. Based on the number of wrinkles generated, there was a possibility of a complex bifurcation structure with numerous equilibrium paths. Additionally, the existence of symmetry described by a dihedral group indicates three more solutions for each solution obtained, implying a multiplicity of the solution

and additional equilibrium points. However, the wrinkle generation mechanism without bifurcations reduces the number of equilibrium paths. Furthermore, the symmetry between deformation patterns reduces the number of possible wrinkle configurations. The number of possible wrinkle configurations is reduced even further by re-coalesce of equilibrium paths occurring after bifurcations. Finally, the membrane bifurcation structure is less complex than it potentially could have been.

The universality of the behavior discussed in this study depends on the universality of the stress field that causes the behavior. Wrinkle generation without bifurcations is caused by the transition between uniaxial compression and biaxial tension. For real systems, effects of gravity, creases, imperfections, and other conditions need to be considered. Therefore, any set of conditions that maintain uniaxial compression and biaxial tension would have this type of wrinkle generation.

References

[1] Chmielewsk,A. B., "Overview of Gossamer Structures," *Gossamer Spacecraft: Membrane and Inflatable Structures Technology for Space Applications*, edited by C. H. M. Jenkins, Vol. 191, Progress in Astronautics and Aeronautics, AIAA, Reston, VA, 2001, pp.1-20.

[2] Senda, K., Oda, T., Ota, S., Igarashi, Y., Watanabe, A., Hori, T., Ito, H., Tsunoda, H., and Watanabe, K., "Deploy Experiment of Inflatable Tube using Work Hardening," *Proc. of AIAA Gossamer Spacecraft Forum*, AIAA-2006-1808, Newport, RI, 2006, pp.1-18.

[3] Timoshenko, S.P. and Gere, J.M., "Bending of Thin Plates," *Theory of Elastic Stability* 2nd ed., Springer, New York, 2010, pp. 319-346.

[4] Wong, Y.W. and Pellegrino, S., "Wrinkled Membranes, Part I," *Journal of Mechanics of Materials and Structures*, Vol. 1, No. 1, Jan. 2006, pp.3-25.

[5] Wong, Y.W. and Pellegrino, S., "Wrinkled Membranes, Part II," *Journal of Mechanics of Materials and Structures*, Vol. 1, No. 1, Jan. 2006, pp.27-61.

[6] Wong, Y.W. and Pellegrino, S., "Wrinkled Membranes, Part III," *Journal of Mechanics of Materials and Structures*, Vol. 1, No. 1, Jan. 2006, pp.63–95.

[7] Miller, R.K. and Hedgepeth, J.M., "An Algorithm for Finite Element Analysis of Partly Wrinkled Membranes," *AIAA Journal*, Vol. 20, No. 12, 1982, pp.1761-1763. doi: 10.2514/3.8018

[8] Miller, R.K., Hedgepeth, J.M., Weingarten, V.I., Das, P., and Kahyai, S., "Finite Element Analysis of Partly Wrinkled Membranes," *Computers & Structures*, Vol. 20, Nos. 1-3, 1985, pp.631-639. doi: 10.1016/0045-7949(85)90111-7

[9] Miyazaki, Y., "Wrinkle/Slack Model and Finite Element Dynamics of Membrane," *International Journal for Numerical Methods in Engineering*, Vol. 66, No. 7, 2006, pp.1179-1209.
doi: 10.1002/nme.1588

[10] Bazant, Z.P. and Cedelon, L., "Buckling of Elastic Frames by Equilibrium Analysis," *Stability of Structures*, Oxford University Press, New York, 1991, pp. 53-73.

[11] Wang, C.G., Du, X.W., Tan, H.F. and He, X.D., "A New Computational Method for Wrinkling Analysis of Gossamer Space Structures," *International Journal of Solids and Structures*, Vol. 46, No. 6, March 2009, pp. 1516-1526.
doi: 10.1016/j.ijsolstr.2008.11.018

[12] Tessler, A., Sleight, D.W., and Wang, J.T., "Effective Modeling and Nonlinear Shell Analysis of Thin Membranes Exhibiting Structural Wrinkling," *Journal of Spacecraft Rockets*, Vol. 42, No. 2, 2005, pp.287-298.
doi: 10.2515/1.3915

[13] Wriggers, P., Wagner, W., Miehe, C., "A Quadratically Convergent Procedure for the Calculation of Stability Points in Finite Element Analysis," *Computer Methods in Applied Mechanics and Engineering*, Vol. 70, No. 3, 1988, pp.329-347.
doi: 10.1016/0045-7825(88)90024-2

[14] Leifer, J., Jones, D.C., Cook, A.M., "Gravity-Induced Wrinkling in Subscale, Singly Curved Parabolic Gossamer Membrane," *Journal of Spacecraft and Rockets*, Vol. 47, No. 1, 2010, pp. 214-219.
doi: 10.2514/1.45672

[15] Woo, K., Jenkins, C.H., "Effect of Crease Orientation on Wrinkle-Crease Interaction for Thin Membranes," *Journal of Spacecraft and Rockets*, Vol. 50, No. 5, 2013, pp. 1024-1034.
doi: 10.2514/1.A32183

[16] Tessler, A., Sleight, D.W., "Geometrically Nonlinear Shell Analysis of Wrinkled Thin-Film Membranes with Stress Concentrations," *Journal of Spacecraft and Rockets*, Vol. 44, No. 3, 2007, pp. 582-588.
doi: 10.2514/1.22913

[17] Inoue, S., "Prediction Methods of Wrinkling in Thin-Membrane," *Proceedings of International Symposium on Space Technology and Science*, Tsukuba, Japan, 2009, pp.1-7.

[18] Senda, K., Nakanishi, K., Takagi, K., "Wrinkle Generation Mechanism without Buckling in Sheared Rectangular Membrane," *Proc. of AIAA Gossamer Spacecraft Forum*, AIAA-2012-1919, Honolulu, HI, 2012, pp.1-30.

[19] Senda, K., Petrovic, M., Nakanishi, K., "Behavior of a Sheared Square Membrane with Cyclic Boundary

Conditions during Wrinkling," *Proc. of AIAA Gossamer Spacecraft Forum*, AIAA-2013-1927, Boston, MA, 2013, pp.1-33.

[20] Endo, A., Hangai, Y., and Kawamata, S., "Post-Buckling Analysis of Elastic Shells of Revolution by the Finite Element Method," *Report of Institute of Industrial Science*, UDC 624.074.4:624.075.4, University of Tokyo, December 1976.

[21] Hoyle, R., "A bit of Group Theory," *Pattern Formation* Cambridge University Press, New York, 2007, pp. 52-84.

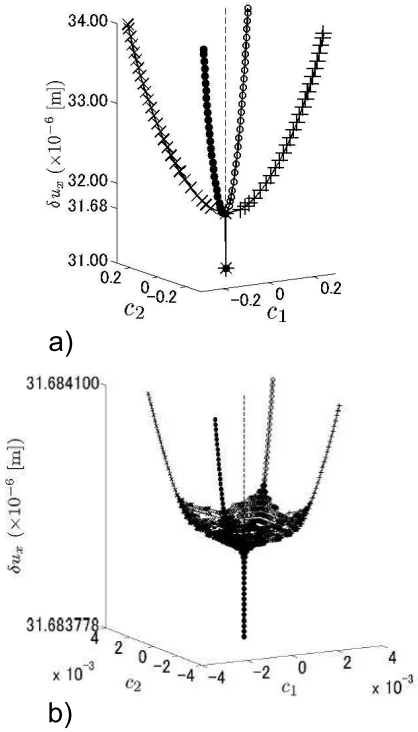

Fig. 4 Bifurcation diagram at Bif. 31.

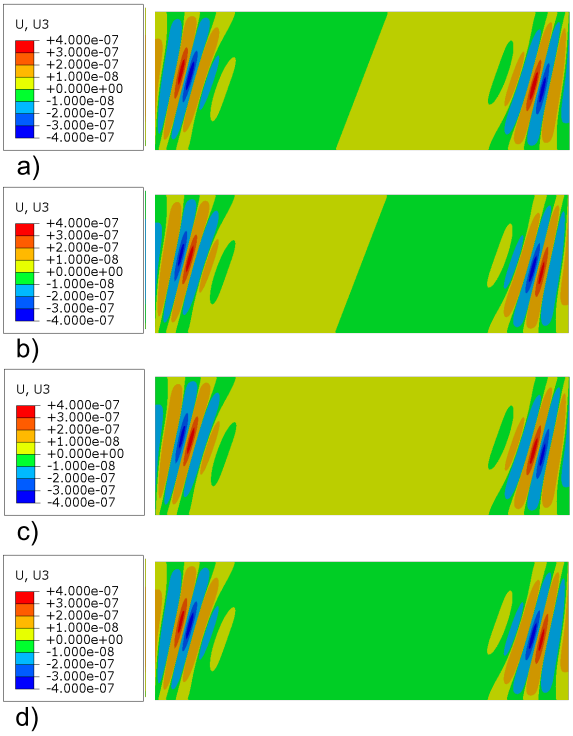

Fig. 5 Wrinkle patterns at $\delta u_x = 31.83 \times 10^{-6}$[m] just after Bif. 31.

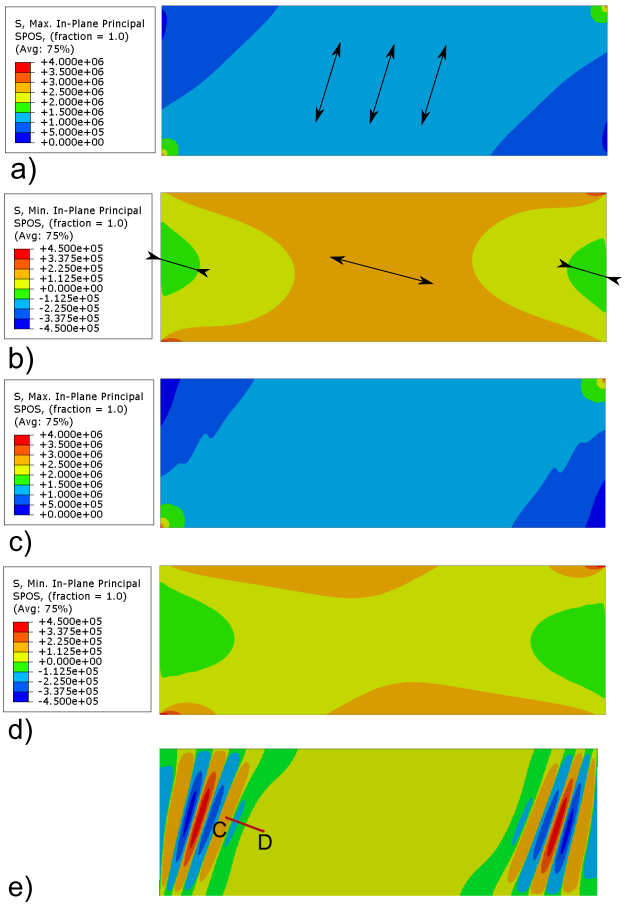

Fig. 6 Principal stress values.

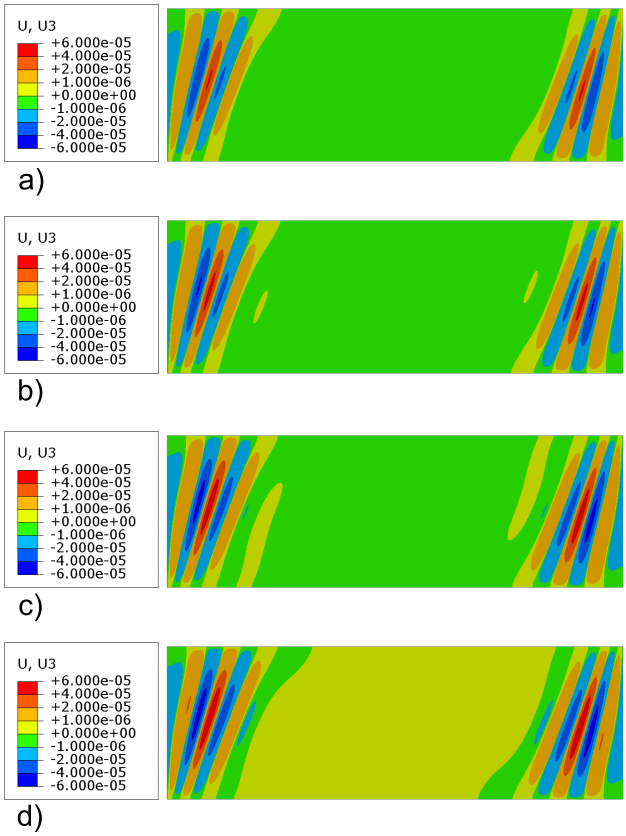

Fig. 7 Wrinkle pattern progression on Path 31-3.

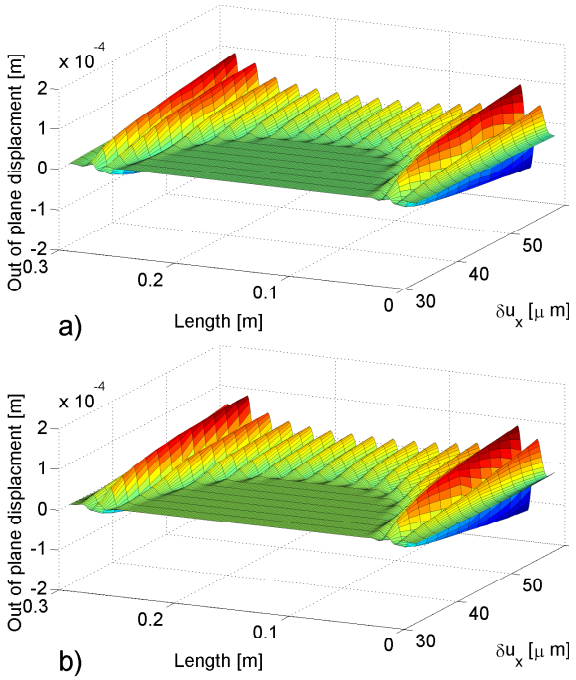

Fig. 8 Wrinkle pattern progression in section AA'.

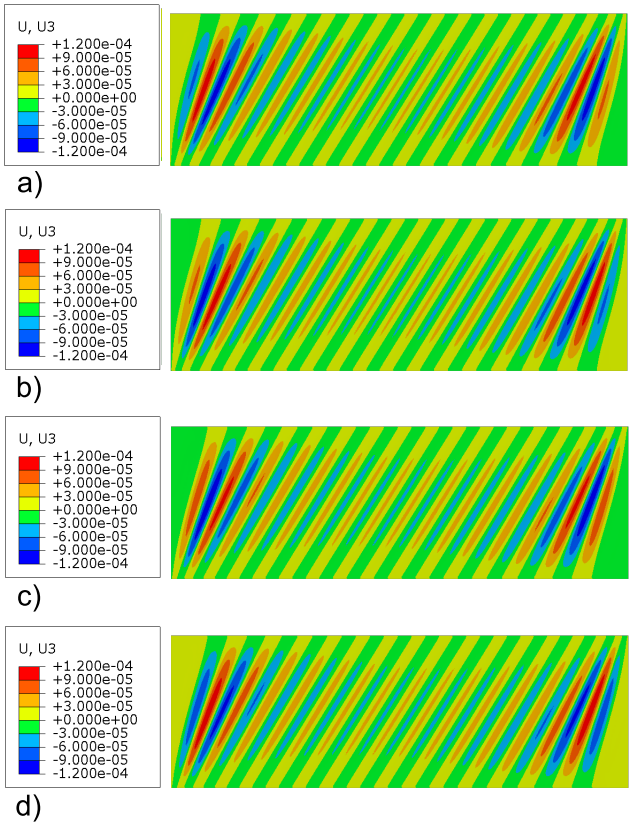

Fig. 9 Wrinkle pattern at $\delta u_x = 60.00 \times 10^{-6}$[m].

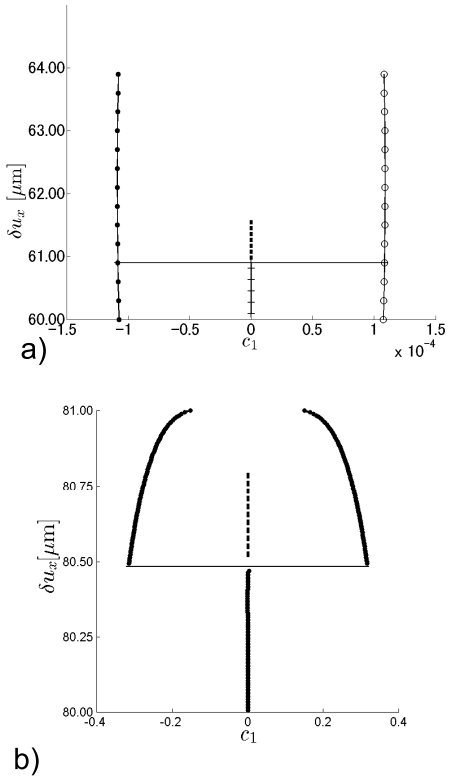

Fig. 10 Bifurcation diagram for Bif. 60 and Bif. 80.

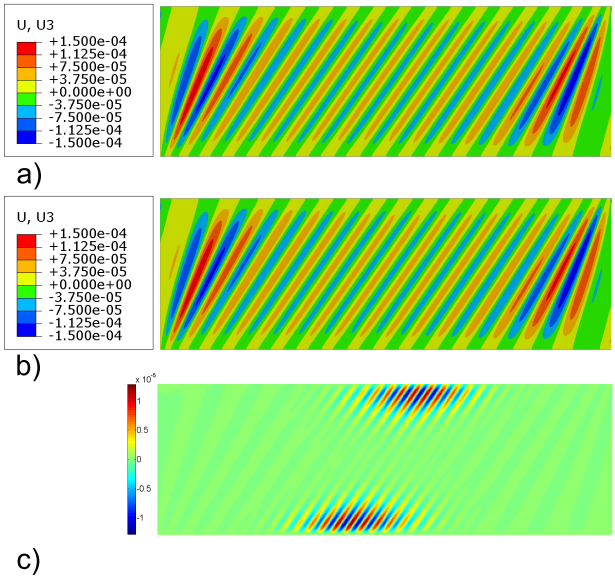

Fig. 11 Paths 80_1-1 and 80_1-2 at $\delta u_x = 81.00 \times 10^{-6}$[m].

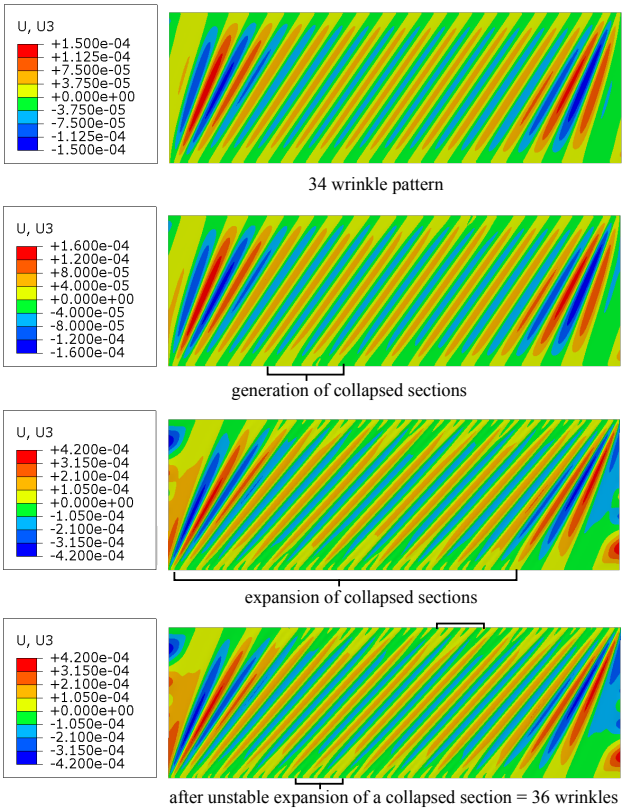

Fig. 12 Wrinkle pattern progression on Path 80_1-1.

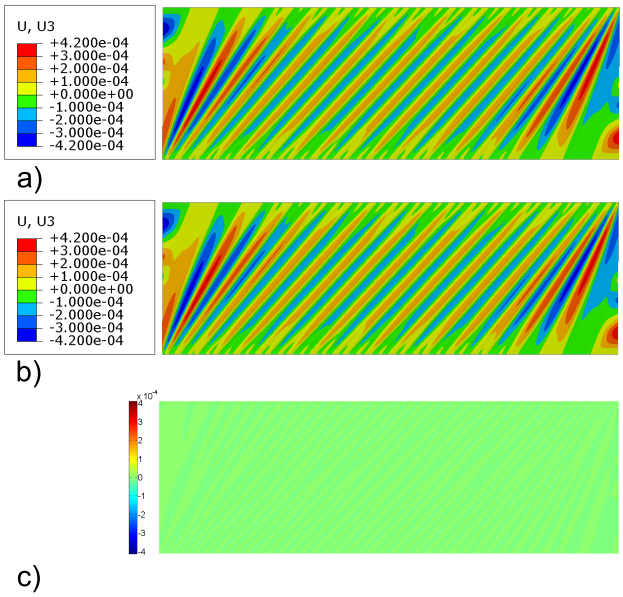

Fig. 13 Paths 80_1-1 and 80_1-2 at $\delta u_x = 440.00 \times 10^{-6}$[m].

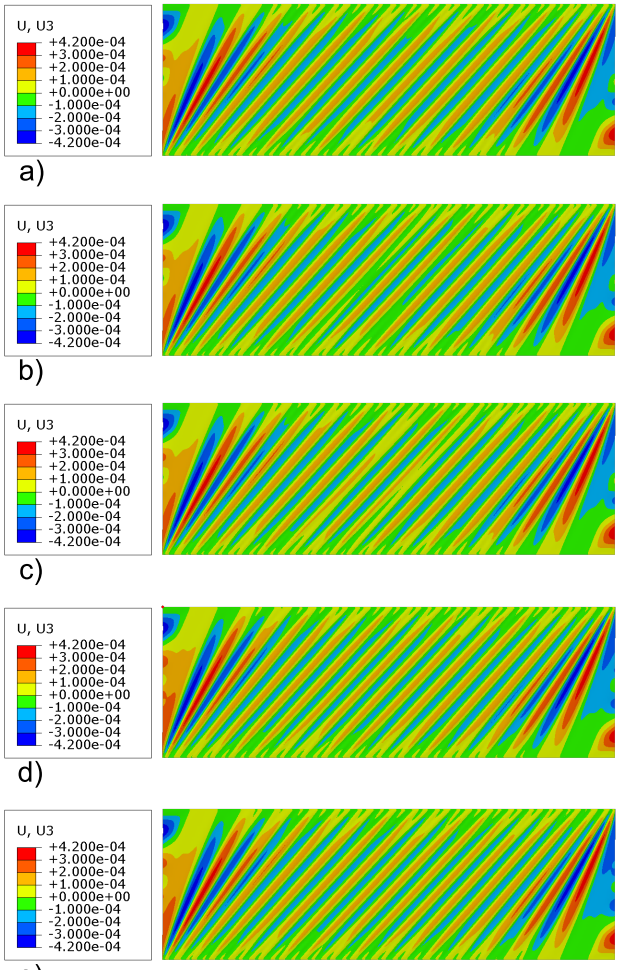

Fig. 14 Bif. 440_1 **wrinkle pattern.**

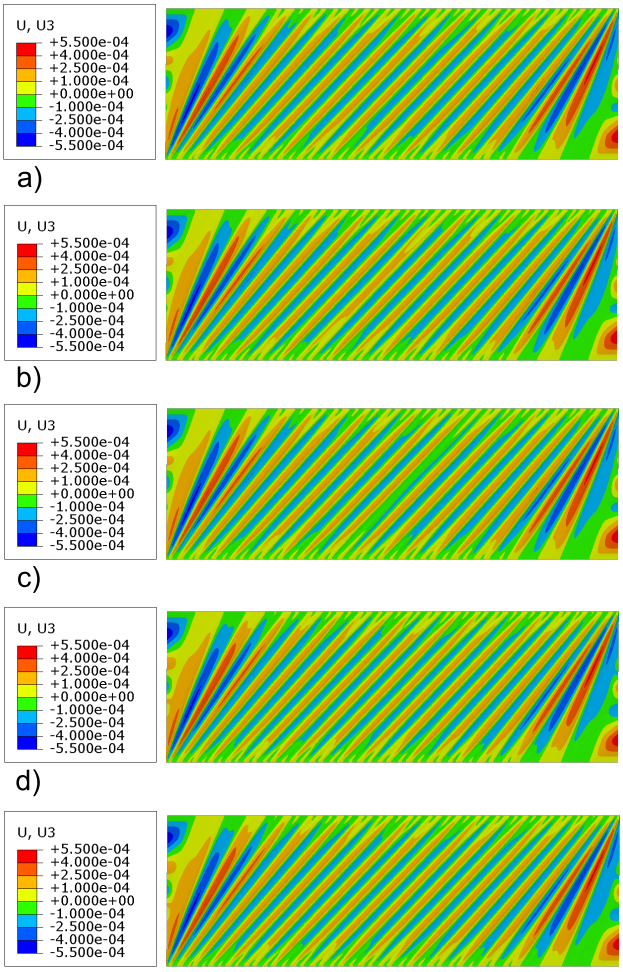

Fig. 15 Bif. 645_1 **wrinkle pattern.**

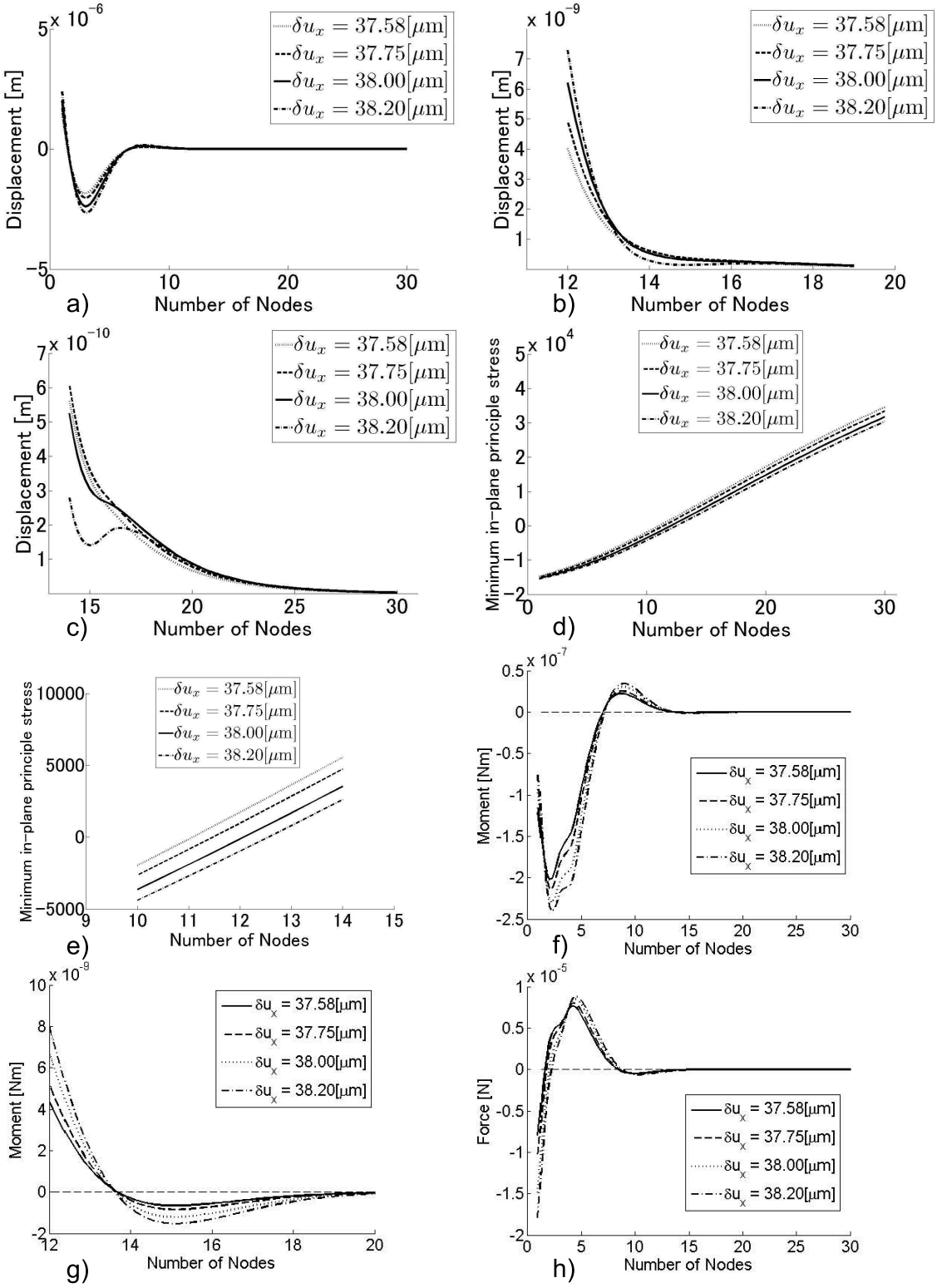

Fig. 16 Path 31-3, wave section analysis.